Electronic Supplementary Material (ESI) for ChemComm.

Electronic Supplementary Information for

Converting *p*-terphenyl into a novel organo-catalyst for LED-driven energy and electron transfer photoreactions in water

M.-S. Bertrams and C. Kerzig

Contents

Department of Chemistry
Johannes Gutenberg University Mainz
Duesbergweg 10–14, 55128 Mainz
Germany
E-mail: ckerzig@uni-mainz.de

1 Experimental section

1.1 General experimental details

All chemicals for optical for optical spectroscopy, preparative experiments and photocatalysis were obtained commercially in high purity and used without further purification (Table S 1).

Table S 1 List of substances used throughout the project, together with their purities and manufacturers.

Compound	**Purity / %**	**Manufacturer**
acetophenone (ACP)	>99	Aldrich
anisaldehyde	>99	TCI
4-benzoylbenzoic acid	99	Aldrich
4-(chloromethyl)benzoic acid	>98	TCI
trans-cinnamylalcohol	98	Aldrich
dodecyltrimethylammonium chloride (DTAC)	99	Aldrich
eosinY	100 weight %	Alfa Aesar
trans-3-fluorocinnamic acid (F-Cin)	98	Aldrich
fuming sulfuric acid	95-99	Fisher Scientific
trans-*N*-methylcinnamylamine	95	ChemBridge
4-methoxybenzyl alcohol	98	Aldrich
potassium acetate	97	Acros Organics
1-pyrenecarboxylic acid	97	Sigma Aldrich
trans-3-(4-pyridyl)acrylic acid	97	Alfa Aesar
sodium ascorbate (NaHAsc)	>99	Aldrich
sodium chloroaceate	98	Aldrich
sodium dodecyl sulfate (SDS)	99	Abcr
sodium hydroxide	>98	Aldrich
sodium 1,5-naphtalenedisulfonate (NDS)	98	TCI
sodium phosphate dibasic	>99	Aldrich
sodium phosphate monobasic monohydrate	>99	Aldrich
sulfuric acid	>95	Acros Organics
riboflavin (vitamin B2)	>98	Sigma Aldrich
p-terphenyl	>99	Acros Organics
trifluoro acetic acid (TFA)	99	Fluorochem
4-(trifluoromehyl)-acetophenone (CF_3-ACP)	98	Abcr
(*R/S*)(1-[4-(trifluoromethyl)phenyl]ethanol	96	Alfa Aesar
tris(2,2′-bipyridyl)dichlororuthenium(II) · 6 H_2O (Rubpy)	99.9	Sigma Aldrich

The solvent used for all synthetic reaction steps, optical spectroscopy and irradiation experiments was ultrapure Millipor MilliQ water (specific resistance 18.2 MΩ cm). Acetonitrile (99.9 %, VWR) and MeOH (>99.8%, HPLC grade from Fisher Chemicals) were used for purification purposes. The solutions for optical spectroscopy, except indicated otherwise, were purged with argon (4.8, PanGas or 5.0, Nippon Gases) or high-quality nitrogen from the general nitrogen supply of the university for 5 minutes before the measurements and sealed under inert gas (1 atm) in septum cap cuvettes.

NMR spectra of **SO_2TDS** and TDS were recorded on a *Bruker Avance III* 500 MHz or a *Bruker Avance II* 400 MHz at 298 K and for the irradiation experiments *Bruker Avance III* HD 300 MHz and *Bruker Avance II* 400 MHz instruments were used. The deuterated solvents for NMR experiments were used as follows: D_2O from Cambridge Isotope Laboratories, Inc. (99.5 %) or from DEUTERO (99.9 %), DMSO-d_6 from Cambridge Isotope Laboratories, Inc. (99.5 %, ^{13}C NMR) and NaOD solution (40 wt% in D_2O 99.5 %) from Aldrich. ^{1}H NMR spectra in D_2O were referenced using the solvent peak (δ = 4.79 ppm).[1] ^{13}C NMR spectra measured

in DMSO-d_6 or D_2O were referenced using the solvent peak of DMSO-d_6 (δ = 39.39 ppm).[1] TFA was used as reference compound for ^{19}F NMR spectroscopy (δ = −76.2 ppm).[2]
ESI mass spectra were recorded on a Di-ESI-MS 8030 Plus instrument (Shimadzu).

Steady-state measurements

Absorption spectra were recorded using a Cary 5000 spectrophotometer from Varian or a LAMBDA 365 from Perkin Elmer. Emission measurements were carried out with a Fluorolog-3-22 from Horiba Jobin-Yvon or a FL-6500 from Perkin Elmer. All steady-state absorption and emission measurements were performed at room temperature (295 ± 2 K) and the emission spectra were corrected for the wavelength-dependent sensitivity of the respective emission spectrometer. Very low concentrations of the emissive compounds were employed to avoid filter effects.[3]

$E_{0,0}$ energies were determined from the intersections of the respective absorption and emission spectra. The **fluorescence quantum yields** were measured against known standard compounds (*p*-terphenyl in cyclohexane[3] for TDS and anthracene in EtOH[3] for **SO_2TDS**). To avoid filter effects,[3] the absorption was adjusted below 0.1 at the excitation wavelengths and in the overlap region of absorption and luminescence spectra. Emission spectra were measured at three different excitation wavelengths, out of which the average value was calculated. Finally, two correction factors were included: i) different refractive indices of the solvents and ii) different optical densities at the excitation wavelengths such that the following well-known formula **(Eqn. 1)**[3] was used to determine the fluorescence quantum yields (ϕ ... quantum yield, I ... integrated luminescence intensity, A ... optical density at the excitation wavelength and n … refractive index of the solvent; subscript “r” refers to the parameters of the reference compound):

$$\phi = \phi_r \frac{I}{I_r} \frac{A_r}{A} \frac{n^2}{n_r^2}$$

(Eqn. 1)

The fluorescence quantum yields so obtained are 0.98 $\pm$ 0.01 (TDS) and 0.48 $\pm$ 0.01 (**SO_2TDS**), both in argon-saturated aqueous solution.

Time-resolved measurements

The fluorescence lifetimes of TDS and **SO_2TDS** were recorded on a LifeSpec II spectrometer from Edinburgh Instruments (time-correlated single photon counting TCSPC technique) with a pulsed LED peaking at 313 nm as a light source.

For the laser flash photolysis (LFP) measurements an LP920-KS apparatus form Edinburgh Instruments was used. The energy of the 355 nm laser pulse (frequency-tripled Nd:YAG laser from Quantel with ~10 ns pulses) was modified by the Q-switch delay (5 mJ to 12 mJ). Kinetic traces were recorded at a single wavelength with a photomultiplier tube and for measuring transient absorption (TA) spectra an iCCD camera from Andor was employed. Depending on the signal-to-noise ratio, TA spectra were time-integrated between 10 and 100 ns. The **SO_2TDS** concentrations for LFP measurements were adjusted such that the absorptions of the aqueous solutions were between 0.03 and 0.1 at the laser wavelength 355 nm, corresponding to **SO_2TDS** concentrations between 6 μM und 18 μM. Control laser experiments on all suitable quenchers/substrates upon 355 nm excitation in the absence of **SO_2TDS** did not yield any quencher-/substrate-derived signals in the transient absorption traces.

The rate constants k_x for the pertinent decay processes of the singlet excited states of TDS and **SO_2TDS** (fluorescence and intersystem crossing) were calculated with the following formula (τ_{S1} ... lifetime of the excited singlet state and ϕ_x…quantum yield of the decay process under study):[3]

$$k_x = \frac{\phi_x}{\tau_{S1}}$$
(Eqn. 2)

To determine quenching rate constants, **Stern-Volmer** analyses of the quenching experiments were performed. The τ_0/τ values from LFP or TCSPC studies were plotted against the concentration of the quencher. A linear fit with the intersection fixed at 1 yielded the Stern-Volmer constant (K_{SV}) and division by the known τ_0 lifetime of the respective excited state under given conditions resulted in the bimolecular quenching rate constant.[3] All lifetimes used for kinetic analyses of bimolecular reactions were measured under pseudo first-order conditions and these lifetimes were derived by monoexponential fits. Examples are given in Figs. S 4 c) and S 6 b) (inset).

1.2 Synthetic procedures and characterization data

Disodium *p*-terphenyldisulfonate (TDS)

The synthesis of TDS has been reported recently by us,[4] because we investigated its properties for photon upconversion in water. However, we largely reproduce the synthetic procedure in the following paragraph for clarity.

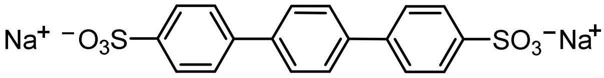

H_2SO_4 (95 %, 8.0 mL, 143 mmol, 7.1 eq.) was heated to 110 °C and *p*-terphenyl (4.60 g, 20.0 mmol, 1.0 eq.) was added portion-wise. After stirring for 4.5 h at 160 °C, the reaction mixture was allowed to cool to rt. H_2O (100 mL) was poured into the reaction mixture and the solution was filtered over Celite. The filtrate was adjusted to pH 6-7 (aq. NaOH, 1.75 M) and a precipitate formed. This mixture was then heated to 95 °C and upon addition of H_2O (1.0 L) a dim solution was obtained which was stirred overnight at 95 °C. Cooling to rt initiated precipitation of the product, which was filtered off and dried *in vacuo* yielding TDS as an off-white powder (6.86 g, 15.8 mmol, 79%). ^1H NMR data obtained in D_2O are in agreement with those presented in ref.[5].

Further purification for optical spectroscopy was performed by dissolving a small amount of the crude product (100 mg, 230 µmol) in MilliQ water (10 mL) and heating to 95 °C until a clear solution was obtained. After cooling to rt a precipitate formed, which was filtered, washed with MilliQ water, and dried *in vacuo* to give TDS as a white solid (65 mg, 150 µmol, 65%).

For the NMR spectra of TDS, see Figs. S 23 – S 25.

^1H NMR (500 MHz, 298 K, D_2O): δ = 7.93 – 7.88 (m, 12H) ppm.

^1H NMR (500 MHz, 298 K, DMSO-d_6): δ = 7.78 (s, 4H), 7.69 (s, 8H) ppm.

$^{13}C\{^1H\}$ NMR (126 MHz, 298 K, DMSO-d_6): δ = 147.5, 139.5, 138.8, 127.2, 126.2, 125.9 ppm.

ESI-MS (*m/z*): calcd. for $C_{18}H_{12}O_6S_2$ ([M-2Na$^+$]): 194.0; found: 194.0.

Sulfone-bridged TDS (SO_2TDS)

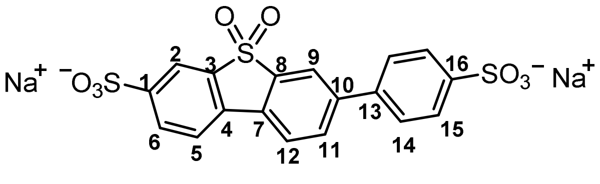

A round bottom flask equipped with a magnetic stirring bar was evacuated and dried, sealed with a septum cap, and kept under inert atmosphere. Fuming sulfuric acid (1.0 ml, 18.8 mmol, 28.8 eq.) was added into the flask. *p*-Terphenyl (150 mg, 0.7 mmol, 1.0 eq.) was added portion-wise under N_2 flow and the mixture was stirred for 3 h at 50 °C. After the reaction mixture was cooled to rt, MilliQ water (4.0 mL, cooled to ~10°C) was poured into the reaction mixture, the solution was filtered over Celite and washed with 1.0 mL of MilliQ water. The filtrate was adjusted to a pH of 6-7 (aq. NaOH, 3.0 M) and precipitation of a colourless solid was initiated. After 4 days of precipitation the solid was filtered off and washed with ice-cooled (0 °C) MilliQ water (2.0 mL) yielding an off-white solid (213 mg, 57 %). The reaction was carried out several times with similar yields. Further purification was performed by suspending 200 mg of the solid raw product in a 15 mL mixture of H_2O and MeOH (1:2) and after vigorous stirring for 30 min the solid was filtered off. The mother liquor was evaporated, and the white solid so obtained was dried at 35 °C under reduced pressure yielding a white solid (120 mg, 60 %; overall yield 34 %). NMR signals have been assigned using 2D NMR spectra (see Figs. S 26 – S 29).

^1H NMR (500 MHz, 298 K, D_2O): δ = 8.18 (d, 1H, J_{HH} = 1.8 Hz, **H2**), 8.05 (dd, 1H, J_{HH} = 8.1 Hz, J_{HH} = 1.8 Hz, **H6**), 7.98 (pseudo-s, 1H, **H9**), 7.88 (d, 1H, J_{HH} = 8.1 Hz, **H5**), 7.83 (m, 2H, **H14**), 7.81 (m, 1H, **H11**), 7.75 (d, 1H, **H12**), 7.64 (m, 2H, **H15**) ppm.
^{13}C {^1H}NMR (126 MHz, 298 K, D_2O): δ = 145.4 (**C3**), 142.8 (**C16**), 142.3 (**C13**), 140.4 (**C10**), 136.9 (**C7**), 136.4 (**C4**), 133.3 (**C11**), 133.2 (**C1**), 132.2 (**C6**), 129.5 (**C8**), 127.1 (**C15**), 126.3 (**C14**), 123.1 (**C12**), 122,9 (**C5**), 120.4 (**C9**), 119.4 (**C2**) ppm.
^{13}C {^1H}NMR (100 MHz, 298 K, DMSO-d_6): δ = 150.6, 148.3, 142.4, 138.5, 137.8, 136.9, 132.9, 131.6, 130.7, 129.5, 126.5, 126.4, 123.6, 122.8, 120.0, 118.8 ppm.
ESI-MS (*m/z*): calcd. for $C_{18}H_{10}O_8S_3$ ([M-2Na$^+$]): 225.0; found: 225.0.

Elemental analysis of TDS and **SO_2TDS** could not be carried out owing to incomplete combustion of the salts. However, quantitative NMR experiments indicate that the water content of both terphenyl-derived compounds is below 10%.

2 Singlet and triplet excited states of **SO_2TDS**

2.1 Singlet quenching of **SO_2TDS**

To ensure that the triplet state is the key species for the photocatalytic activity of **SO_2TDS,** additional singlet quenching experiments were performed (Fig. S 1). The radical anion **$SO_2TDS^{\bullet-}$** for the mechanistic studies on pinacol coupling reactions was generated through triplet state quenching by HAsc$^-$ (see main paper and Section 3), but the driving force for the corresponding **$^1SO_2TDS^*$** reduction is much higher. Hence, we also investigated the quenching behaviour of **$^1SO_2TDS^*$** in the presence of HAsc$^-$ (Fig. S 1). Our measurements of the singlet lifetime with increasing HAsc$^-$ concentrations yielded a linear Stern-Volmer plot and a diffusion-controlled quenching rate constant taking Coulombic repulsion into account (2.2×10^9 $M^{-1}s^{-1}$). Owing to the short lifetime of **$^1SO_2TDS^*$** (as opposed to ^{3}**SO_2TDS**), the actual efficiency of reductive singlet state quenching is below 20 % under the conditions employed for photocatalysis experiments (HAsc$^-$ concentrations between 10 mM and 20 mM). On the other hand, triplet quenching by HAsc$^-$ already occurs with an efficiency close to unity (> 99 %) at quencher concentrations as low as 0.3 mM. In addition to the kinetics that predict a predominant triplet photoreduction under our conditions, the small fraction of reductive singlet state quenching does not necessarily contribute to the overall formation of **$SO_2TDS^{\bullet-}$**, given that the inherent yield of photoinduced electron transfer reactions with singlet states is usually low as a result of unproductive in-cage recombination.[6–8] Quantitative LFP experiments monitoring the **$SO_2TDS^{\bullet-}$** formation with different HAsc$^-$ concentrations (up to 20 mM) did not show a signal increase at higher quencher concentrations (i.e., under conditions with quantitative triplet quenching and additional singlet quenching). We, therefore, exclude productive quenching of **$^1SO_2TDS^*$** by HAsc$^-$ in our system and the catalyst triplet is indeed the key species (see main paper and Section 3.1 for its productive quenching by HAsc⁻).

Similar kinetic estimations and control experiments with the model substrate F-Cin revealed that ^{3}**SO$_2$TDS** is the key species for the lab-scale isomerization reactions as well.

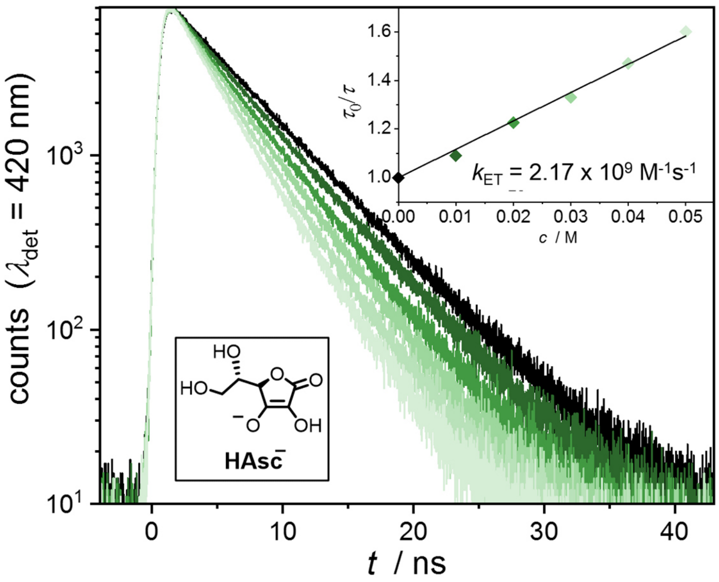

Fig. S 1 Lifetime changes of ^{1}**SO$_2$TDS*** (λ_{exc} = 313 nm and λ_{det} = 420 nm) in aqueous phosphate buffer (20 mM at pH 7.2) with increasing (lighter green) HAsc⁻ (sodium salt) concentrations. Inset: corresponding Stern-Volmer plot (same color code) and resulting quenching rate constant.

2.2 Triplet lifetime

In bimolecular quenching reactions with charged species, the concentration of ions in solution can modify the rate constant significantly. This so-called kinetic salt effect can be approximated by the Brønsted-Bjerrum equation and several studies address this effect in literature,[9–15] but it is only valid at rather low ionic strengths of the solutions. For the LFP quenching experiments (see following sections), the solutions were usually prepared in phosphate buffer, such that the addition of the (ionic) quencher would not modify the ionic strength drastically, and the electron or energy transfer rate constant is not influenced by this effect. As expected, the lifetimes of ^{3}**SO$_2$TDS** also varied depending on the ionic strength (concentration of phosphate buffer and **SO$_2$TDS** itself) of the solution. Furthermore, with a long integration time and suppressing the detection of prompt fluorescence by a sufficiently long delay time, we detected delayed ^{1}**SO$_2$TDS*** fluorescence in the time-gated emission spectra. This finding is indicative for triplet-triplet annihilation (TTA) of two ^{3}**SO$_2$TDS** species thereby adding a second order decay pathway, which is, however, rather inefficient under our conditions.

Both effects complicate the exact determination of the triplet lifetime. Keeping this in mind, the respective τ_0 values were determined individually before starting the LFP quenching experiments. Moreover, for all LFP experiments that required more than one sample, stock solutions containing the buffer and **SO$_2$TDS** (and HAsc⁻ for Section 3.2) were used such that the ionic strength within one series of measurements remained as equal as possible.

All unquenched triplet lifetimes that were measured throughout the LFP experiments exceeded 100 µs, which is why this value is given as lower limit for the lifetime of ^{3}**SO$_2$TDS** (Table 1 of the main paper).

2.3 LFP quenching studies with NDS

NDS is a known water-soluble triplet energy acceptor and has been investigated thoroughly concerning its triplet-triplet absorption spectrum, triplet energy and extinction coefficients.[4,16–18] For a detailed analysis of the formed species observed in the TA spectrum upon 355 nm excitation of **SO_2TDS**, we performed LFP quenching experiments with NDS (Figs. S 2 and S 4). DFT calculations predict that the triplet energies are close (Sections 4 and 5) and therefore a triplet-triplet energy transfer (TTET) is thermodynamically possible. Initially we observed the decrease of the **$^3SO_2$TDS** lifetime with increasing NDS concentrations and from the obtained data we performed a Stern-Volmer analysis and calculated a k_{TTET} of 7.3×10^6 $M^{-1}s^{-1}$ (Fig. S 2 b), c)). This TTET rate constant is three orders of magnitude below the diffusion limit (~ 5×10^9 $M^{-1}s^{-1}$; for uncharged species)[3] and a brief discussion of the TTET kinetics is given in Section 5. For the TA spectrum of ^{3}NDS measured after TTET from **$^3SO_2$TDS**, see main paper and Fig. S 4.

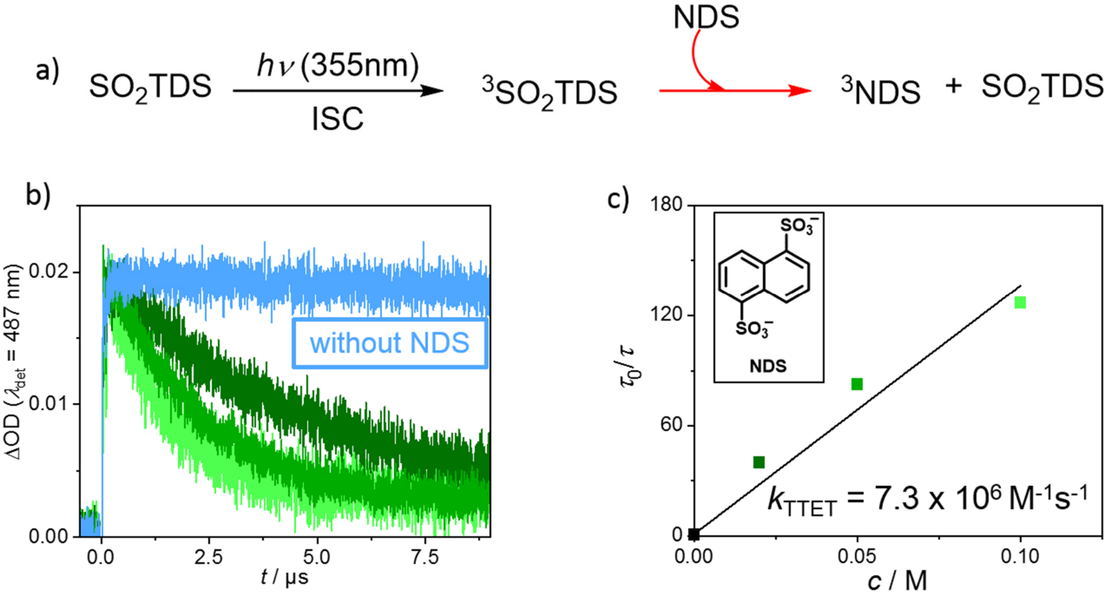

Fig. S 2 LFP quenching of **$^3SO_2$TDS** with NDS: a) Reaction scheme with excitation wavelength (355 nm, 8 mJ) and the observed quenching reaction indicated by the red arrows. b) Kinetic traces monitoring **$^3SO_2$TDS** at 487 nm without NDS (blue) and with increasing NDS concentrations (high concentrations correspond to lighter green). c) Stern-Volmer plot, together with the resulting quenching constant k_{TTET}. For a TA spectrum of the quenching product ^{3}NDS, see main paper or Fig. S 4. All solutions (10 mM phosphate buffer at pH 7.2) were degassed with Ar for 5 min.

2.4 LFP quenching studies with F-Cin

Having established the optical properties of the **$^3SO_2$TDS** species with LFP studies, we further investigated the quenching of this triplet excited state by F-Cin. In the irradiation experiments we observed a *cis*/*trans* isomerization leading to a photostationary state (see main paper and Section 6.5). Previously (Section 2.1), we established that **$^1SO_2$TDS*** is not quenched by F-Cin employed at concentrations of a few mM, which is why the triplet excited state was suggested to initiate the isomerization with a TTET as the underlying mechanism. LPF quenching studies confirmed this hypothesis and efficient triplet quenching was indeed observed: The lifetime of **$^3SO_2$TDS** (after direct excitation of **SO_2TDS** at 355 nm and ISC, see Fig. S 3) was monitored at the absorption maximum (λ_{det} = 485 nm) in the absence of a quencher (blue trace) and with increasing quencher concentration (F-Cin, red traces, Fig. S 3 c). The lifetimes were analysed using a Stern-Volmer plot and a rate constant for the TTET (k_{TTET} = 1.8×10^9 $M^{-1}s^{-1}$) close to the diffusion limit was extracted. Additional TA spectra after a time delay of 6 µs did not show any absorbing species, which is in line with complete

^{3}SO$_2$TDS quenching (see black trace in the inset of Fig. S 3 c)). The expected quencher-derived product, ^{3}F-Cin, could not be detected, indicating that the triplet of this olefinic substrate is a short-lived species. Similar observations have been made for (perpendicular) triplets of other compounds containing isomerizable double bonds.[19]

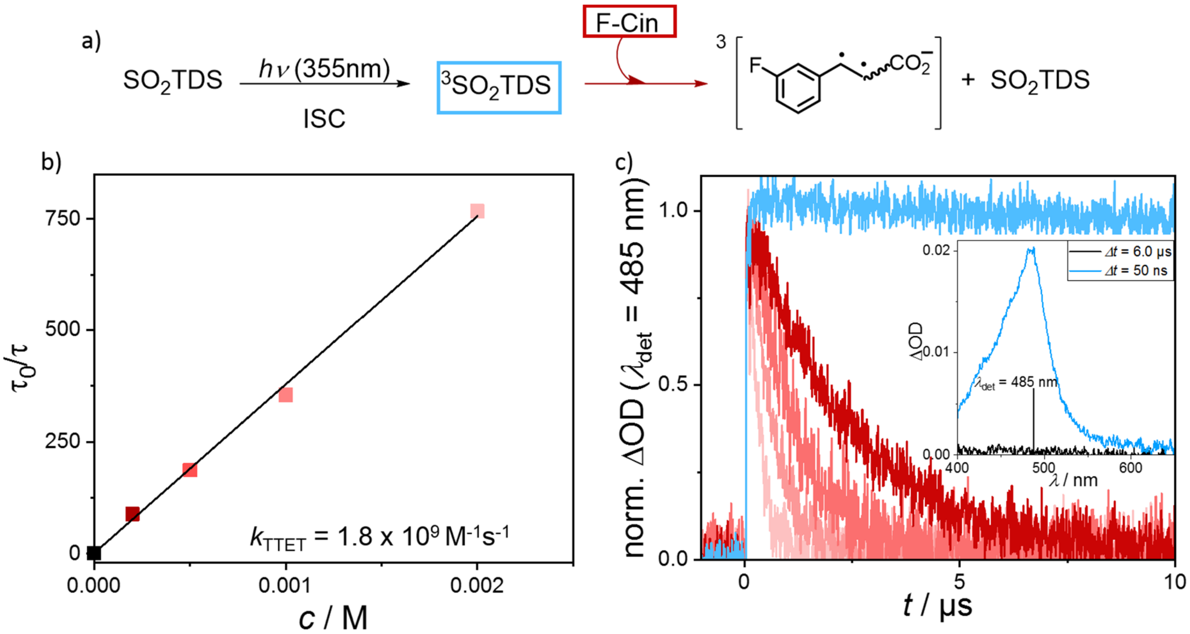

Fig. S 3 LFP quenching of **^{3}SO$_2$TDS** with F-Cin: a) Scheme of the reaction sequence under investigation with the observed quenching reaction highlighted with red arrows. b) Stern-Volmer plot of the quenching experiments with increasing F-Cin concentrations (lighter color). c) Main plot: Kinetic traces (excitation at λ_{exc} = 355nm, 9 mJ) detected at λ_{det} = 485 nm of the unquenched (blue) **^{3}SO$_2$TDS** with increasing F-Cin concentrations (high concentrations correspond to lighter color). Inset: TA spectra of **^{3}SO$_2$TDS** with 0.5 mM F-Cin measured after a time delay of 50 ns (blue) and 6.0 µs (black). All aqueous solutions (50 mM phosphate buffer at pH 7.2) were degassed with Ar for 5 min prior to the experiments.

2.5 ISC quantum yield of **SO$_2$TDS**

The unknown ISC quantum yield (ϕ_{ISC}) of **SO$_2$TDS** was estimated with a Rubpy (ruthenium-tris(2,2'-bipyridin)) reference sample (ϕ_{ISC} = 1)[20] employing relative actinometry.[16,21] Both solutions were adjusted to an absorption of about 0.1 at the excitation wavelength (λ_{exc} = 355 nm, slight differences will be considered later in this section) ensuring practically identical concentrations of (singlet) excited states right after the laser pulse. The exact triplet state concentrations can be calculated with the *Beer-Lambert* law using the TA absorption signal(s), but this is only possible for compounds with known extinction coefficients of the triplet-excited species. For Rubpy the $\Delta\varepsilon$ (i.e. the difference extinction coefficient between ground and triplet state) at λ_{det} = 455 nm is literature known (–10 100 M^{-1}cm^{-1}),[22,23] whereas such data set for **^{3}SO$_2$TDS** is unavailable as this species has not been observed so far. For converting **^{3}SO$_2$TDS** into an intermediate that can be quantified, we used NDS present at high concentrations as triplet energy acceptor with a known $\Delta\varepsilon$ = 9900 M^{-1}cm^{-1} at λ_{det} = 445 nm.[16] We established that NDS does not absorb at the excitation wavelength[16] (λ_{exc} = 355 nm; compare, absorption spectra shown in Section 6.2) but quenches **^{3}SO$_2$TDS** such that the detected ^{3}NDS in solution can only originate from a TTET (Scheme S1).

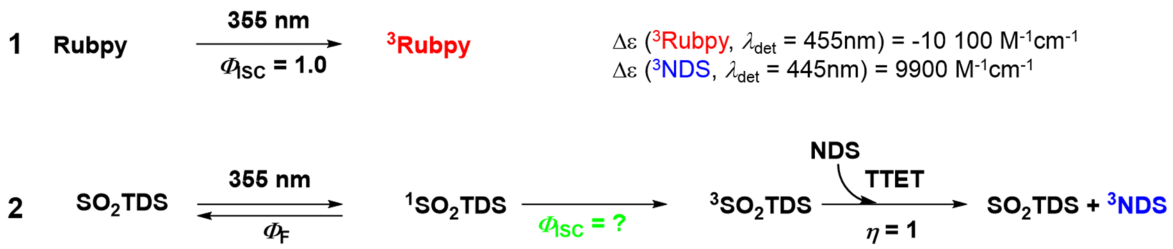

Scheme S1 Reaction scheme for relative actinometry with the Rubpy (1) reference system and the solution with **SO_2TDS** and NDS (2) as triplet energy acceptor with known extinction coefficient of the triplet excited state. The unknown ϕ_{ISC} is highlighted in green.

With that methodology, we can assume that the initial concentration of **$^3SO_2TDS$** right after ISC equals the ^{3}NDS concentration (after quenching) under the given conditions ensuring quantitative TTET (> 99 %). This not only allows the indirect calculation of the quantum yield of **$^3SO_2TDS$** but also the determination of the extinction coefficient of that species:

The ratio of the triplet quantum yields equals the ratio of the concentrations of the triplet excited species, which again can be determined using the *Beer-Lambert* law. Thus, the following equation **(Eqn. 3)** can be used for estimating ϕ_{ISC} of **SO_2TDS**:

$$\frac{\phi_{\mathrm{ISC}}^{\mathrm{SO_2TDS}}}{\phi_{\mathrm{ISC}}^{\mathrm{Rubpy}}} = \frac{[^3\mathrm{SO_2TDS}]}{[^3\mathrm{Rubpy}]} = \frac{[^3\mathrm{NDS}]}{[^3\mathrm{Rubpy}]} \Rightarrow \phi_{\mathrm{ISC}}^{\mathrm{SO_2TDS}} = \phi_{\mathrm{ISC}}^{\mathrm{Rubpy}} \frac{[^3\mathrm{NDS}]}{[^3\mathrm{Rubpy}]}$$

(Eqn. 3)

The values for the optical densities ΔOD were obtained directly from the kinetic transient absorption traces (Fig. S 4 arrows in b) and c)). As already seen in **Eqn. 1** for a related method, a correction for the known, but slightly different (ground-state) absorptions at the excitation wavelength was considered. The final value for ϕ_{ISC} of **SO_2TDS** including the correction factor (× 1.11) amounts to 34.4 %.

Assuming that [**$^3SO_2TDS$**]=[^{3}NDS] we were able to estimate an extinction coefficient of triplet-excited **SO_2TDS** at the detection wavelength 487 nm: Δε = 20 900 M^{-1}cm^{-1}.

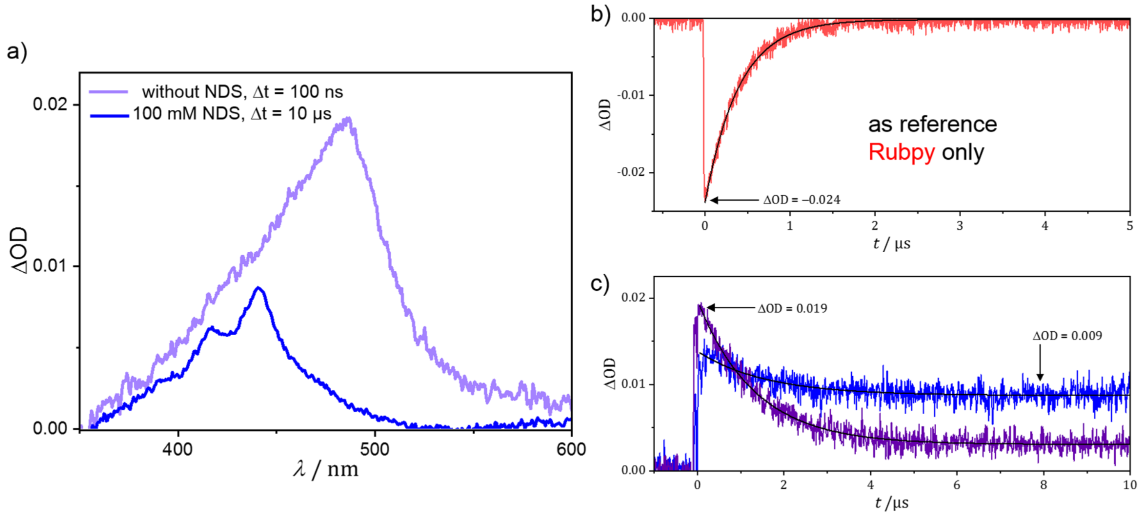

Fig. S 4 Quantitative LFP measurements for calculating ϕ_{ISC} and $\Delta\varepsilon$ of **$^3SO_2TDS$**. The excitation wavelength for all spectra and kinetic traces was λ_{exc} = 355 nm with a constant laser energy of 8 mJ. The solutions were prepared in aqueous NaOH (10 mM) and purged for 5 min with Ar: a) TA spectrum of **$^3SO_2TDS$** (purple, 100 ns time delay) without NDS and in the presence of 100 mM NDS (blue, 10 µs time delay). b) Kinetic trace monitoring the Rubpy bleach recovery at 455 nm. c) Kinetic traces upon excitation of **SO_2TDS** in the presence of NDS (100 mM, same solution as in part a) of the Fig.) detected at 487 nm (purple trace, **$^3SO_2TDS$** decay) and at 445 nm (blue trace, ^{3}NDS formation). The ΔOD values used for the quantum yield calculations were taken from the kinetic traces. Arrows in b) and c) point to the positions that were selected to determine those values. For further explanations, see text.

3 **SO$_2$TDS** radical anion

3.1 Radical anion formation

Besides the observed TTET donor reactivity, our catalyst shows electron transfer reactivity in the presence of the reductive quencher ascorbate HAsc$^-$ (see main paper). The corresponding LFP studies confirming reductive triplet state quenching and the formation of **SO$_2$TDS$^{\bullet-}$** are presented in this section. Upon excitation (355 nm) ^{3}**SO$_2$TDS** is formed, which is subsequently reduced by HAsc$^-$ as sacrificial donor forming the radical anion as indicated by the characteristic spectrum displayed in part a) of Fig. S 5 (purple spectrum). This spectrum shows two absorption maxima (λ_{max} = 485 nm and 700 nm) of similar intensities and the additional absorption band in the red/NIR region (compared to ^{3}**SO$_2$TDS**) is indicative of radical anion formation.[24] The formation rate constant for this species was determined by monitoring the ^{3}**SO$_2$TDS** lifetime decrease upon HAsc$^-$ addition followed by a Stern-Volmer analysis. Both species, the triplet and the radical anion show an absorption band with a maximum around 485 nm but with different extinction coefficients, which is why the kinetic traces of the triplet do not entirely decrease back to the baseline after the quenching process. A rate constant slightly below the diffusion limit (9.7 × 10^8 M^{-1}s^{-1}) was determined at the detection wavelength 485 nm (triplet decay). As a further control experiment, we monitored the formation kinetics of the radical anion at 700 nm (Fig. S 5 c), top), which gave practically the same rate constant for reductive quenching as observed at 485 nm. However, owing to the higher sensitivity of the employed TA instrument at the latter detection wavelength and the resulting much better data quality, we used the kinetic traces recorded at 485 nm for the Stern-Vomer analysis presented in part b) of Fig. S 5.

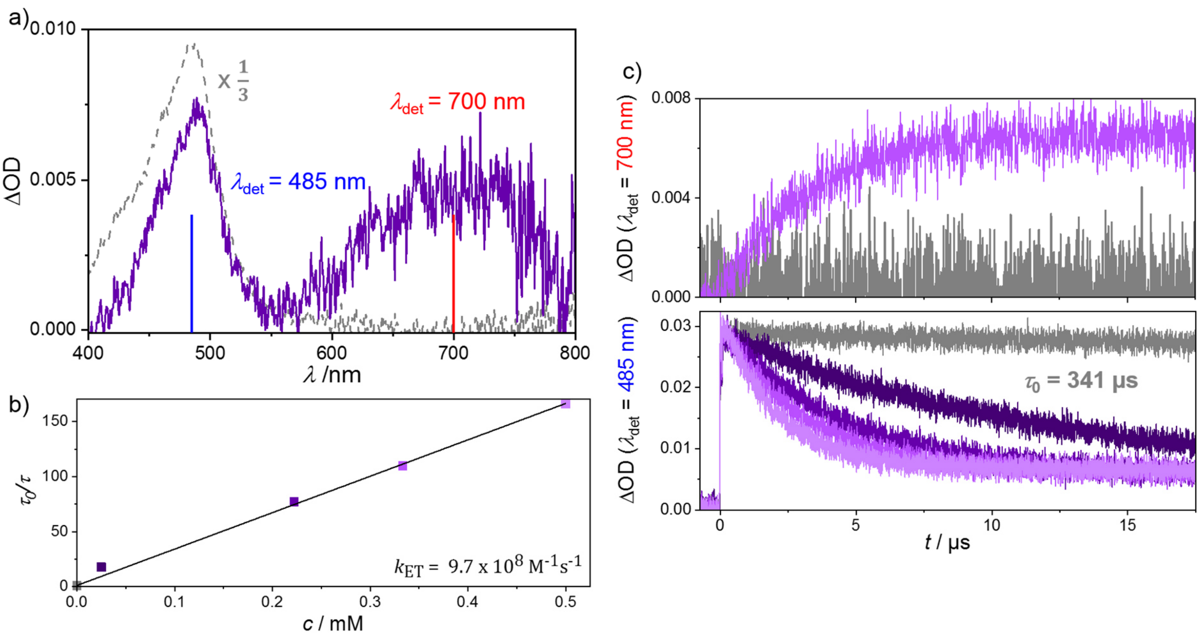

Fig. S 5 LFP experiments on the formation of **SO$_2$TDS$^{\bullet-}$** (λ_{exc} = 355 nm, 6 mJ): a) TA spectrum of the radical anion (aq. solution with **SO$_2$TDS**, 5 mM HAsc$^-$ and 10 mM phosphate buffer at pH 7.2, 5 µs time delay) in purple with ^{3}**SO$_2$TDS** (grey dashed line) for comparison as well as the detection wavelengths of the kinetic traces displayed in part c) of the Fig. b) Stern-Volmer plot and resulting rate constant of the electron transfer (ET) reaction. c) Bottom: Kinetic traces of triplet quenching at λ_{det} = 485 nm with increasing concentrations of HAsc$^-$ (color code as in b)) as well as the unquenched triplet lifetime (grey trace). Top: Sample kinetic trace showing radical anion formation at λ_{det} = 700 nm, same color code as in b). Only one trace in the presence of HAsc$^-$ is shown for clarity. For further explanations, see text.

3.2 Radical anion quenching by ACP

For the final confirmation of the reaction mechanism and $\mathbf{SO_2TDS^{\bullet -}}$ as catalytically active species, we aimed to find spectroscopic evidence of the intermediate produced by the reaction between ACP and the $\mathbf{SO_2TDS}$ radical anion. The TA spectrum of the expected intermediate, the ACP$^{\bullet -}$ species,[25,26] is well known at basic pH. However, under our usual reaction conditions (neutral solution) ACP$^{\bullet -}$ is in a fast equilibrium with the protonated ketyl radical ACPH$^{\bullet}$ (pK_a = 9.6 [25,26], part a) of Fig. S 6). The latter is thus the predominant species at pH ~7. This neutral ACP-derived radical absorbs in the UV region (< 350 nm) overlapping with HAsc^{-} and corresponding quenching or related decomposition products,[16] as well as with $\mathbf{SO_2TDS}$. Thus, detection of the ACP$^{\bullet -}$ or ACPH$^{\bullet}$ is not possible under the standard reaction conditions of the irradiation experiments. Initially, we analyzed the bimolecular quenching of the $\mathbf{SO_2TDS}$ radical anion by ACP at pH 7 yielding the expected linear Stern-Volmer plot and a rate constant of $4.9 \times 10^6\ M^{-1}s^{-1}$ (Fig. S 7). The TA spectra completely return to the baseline in the visible region (Fig. S 6 b) and Fig. S 7 b)), as expected for the formation of ACPH$^{\bullet}$ as final quenching product (compare, Fig. S 6 a)). This situation changes completely at pH 12; under these conditions, the delayed TA spectra show a new absorption band at 445 nm (Fig. S 6 c)), which corresponds to the ACP radical anion as the product of the reaction with $\mathbf{SO_2TDS^{\bullet -}}$. Because of a noticeable extinction coefficient of Asc^{2-}, which is the predominant ascorbate species at pH 12,[15] at our laser wavelength (355 nm), we reduced the overall ascorbate concentration for these measurements on alkaline solutions, and we were indeed able to observe the reaction sequence presented in Fig. S 6 a).

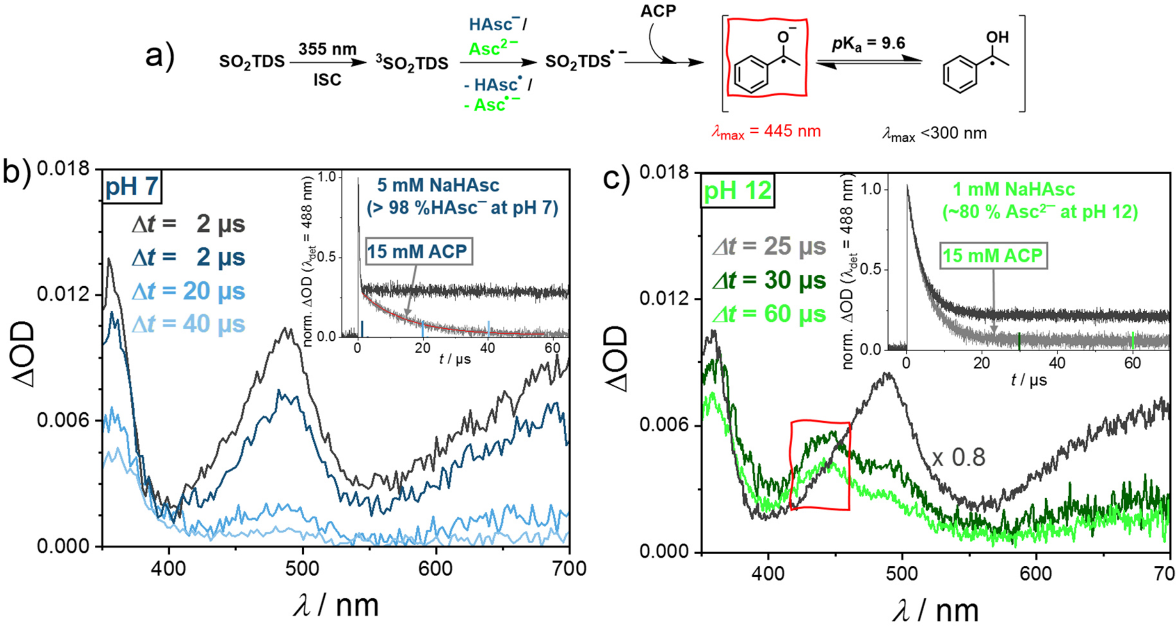

Fig. S 6 Detection of the ACP radical anion[25,26] with pH-dependent LFP experiments: a) Reaction sequence at pH 7 (HAsc^{-}) and pH 12 (Asc^{2-}), molecular structure of the ACP radical anion intermediate (red frame), and the pK_a for the equilibrium with the protonated ketyl radical. b) Main plot: TA spectrum of $\mathbf{SO_2TDS^{\bullet -}}$ at pH 7 (grey) and TA spectra under the same conditions but with ACP (15 mM) added and measured at different delay times (dark blue to light blue). Inset: Kinetic traces monitoring $\mathbf{SO_2TDS^{\bullet -}}$ with (light grey, red line indicates a monoexponential fit) and without ACP (dark gray) with the detection delay times (vertical lines) of the TA spectra in the same color code as in the main plot. c) TA spectrum of $\mathbf{SO_2TDS^{\bullet -}}$ at pH 12 in grey and TA spectra under the same conditions with ACP added, but at different delay times (dark green, 30 µs and light green, 60 µs). In addition to the $\mathbf{SO_2TDS^{\bullet -}}$ absorption bands at 488 nm and 700 nm, we observed a new species in the green spectra with a maximum at 445 nm (red frame), which corresponds to the ACP radical anion. Inset: Kinetic traces monitoring $\mathbf{SO_2TDS^{\bullet -}}$ (dark grey) and its quenching by ACP (light grey). Ascorbate-derived species do not absorb above 400 nm. The initial fast signal decay at 485 nm is due to $\mathbf{SO_2TDS}$ triplet quenching. Triplet quenching is well-separated from $\mathbf{SO_2TDS^{\bullet -}}$ quenching in neutral solution (i.e., under the conditions of Fig. S 7 as well), whereas both quenching processes cannot be separated in alkaline solution. See text for details.

The fact that the **SO$_2$TDS$^{\bullet-}$** absorption bands persist to some extent in the green spectra of part c) in Fig. S 6 (i.e., in the presence of ACP) implies a reversibility of the electron transfer between **SO$_2$TDS$^{\bullet-}$** and ACP.

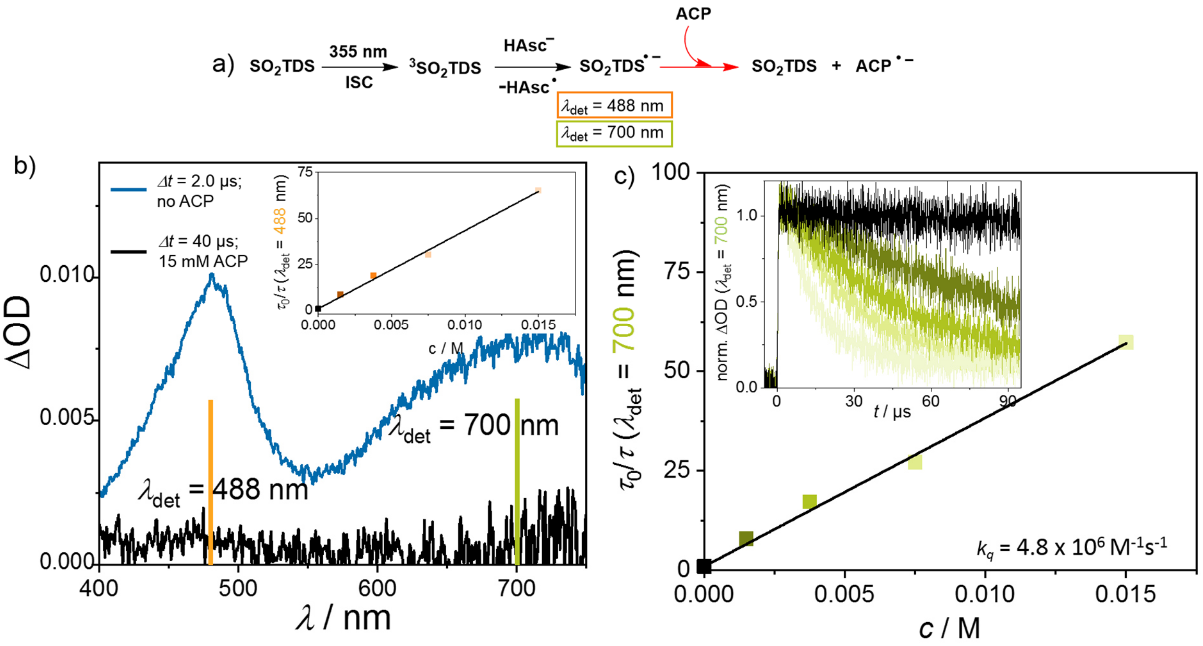

Fig. S 7 Kinetic studies on the reaction between **SO$_2$TDS$^{\bullet-}$** and ACP: a) Reaction scheme with the observed quenching step highlighted by red arrows. b) Main plot: TA spectrum of the radical anion (blue trace, time delay 2 μs, without ACP) and after the addition of 15 mM ACP (black trace, time delay 40 μs; ACP-derived quenching products cannot be observed at neutral pH, which is in perfect agreement with ACP radical anion protonation as displayed in Fig. S 6 a) with the detection wavelengths as vertical lines. Inset: Stern-Volmer analysis of the **SO$_2$TDS$^{\bullet-}$** quenching detected at λ_{det} = 488 nm (k_{q} = 4.9 × 10^6 $\mathrm{M^{-1}s^{-1}}$). c) Main plot: Stern-Volmer plot and corresponding kinetic traces (inset) detected at λ_{det} = 700 nm (k_{q} = 4.8 × 10^6 $\mathrm{M^{-1}s^{-1}}$). All solutions were prepared in aq. phosphate buffer (200 mM, pH 7.2) and a standardized HAsc$^-$ concentration (5.0 mM) was employed.

4 Quantum-mechanical computations

All DFT calculations were carried out with the Gaussian 09 software package[27] using the B3LYP functional in combination with the 6-31+G(d,p) basis set. The solvation model was IEFPCM with water as solvent. The geometry optimizations of *p*-terphenyl and the derivatives under study were accompanied by frequency analyses. The optimized structures used for further computations did not show negative vibrational frequencies, indicating convergence on minimum structures. The frontier orbitals of the singlet ground states were obtained by additional single-point calculations with population analyses, and time-dependent DFT computations with identical functional and basis were used to calculate vertical excitation energies as well as oscillator strengths.

Starting from the energy-minimized singlet ground state geometries, the corresponding lowest triplet states and radical anions were calculated. The triplet state energies were determined simply by comparing the energies of both optimized structures (i.e., singlet ground state and triplet state) for a given compound.[14,28–30] Optimized structures, frontier orbitals and spin densities for the relevant intermediates derived from *p*-terphenyl, TDS and **SO$_2$TDS** are displayed in Fig. S 8 and Fig. S 9. Pertinent energies are summarized in Table S 2. All results clearly indicate that the computed and experimental (see main paper) properties for *p*-terphenyl and TDS are almost identical. Computationally, **SO$_2$TDS** shows substantial differences in terms of spin density and orbital coefficient distributions, orbital energies as well as vertical excitation energies. The smaller HOMO-LUMO gap for **SO$_2$TDS** (and the lower $E_{0,0}$ accordingly) can be explained by a significant LUMO stabilization owing to the sulfone group, as our comparative orbital energy analysis revealed.

Table S 2 Pertinent computed energies (in eV) and oscillator strengths for TDS and **SO_2TDS** relative to those of the parent compound *p*-terphenyl.

	***p*-terphenyl**	**TDS**	**Δ*E* (TDS) [e]**	**SO_2TDS**	**Δ*E* (SO_2TDS) [e]**
$E_{0,0}$ (DFT) [a]	4.17	4.02	−0.15	3.56	−0.61
$E_{0,0}$ (exp.) [b]	3.99	3.75	−0.24	3.37	−0.62
Δ*E* (HOMO-LUMO) [c]	4.61	4.49	−0.12	4.10	−0.51
***f* (HOMO-LUMO) [d]**	1.06	1.38	+0.32	0.66	−0.40
E_T	2.62[f]	2.60	−0.02	2.47	−0.15

[a] Vertical excitation energies. [b] Experimental results, see Fig. 1 and Table 1 of the main paper for details. [c] HOMO-LUMO gap. [d] Oscillator strength of the HOMO-LUMO transition. [e] Comparison with *p*-terphenyl. [f] Experimental triplet energy, 2.53 eV.[3]

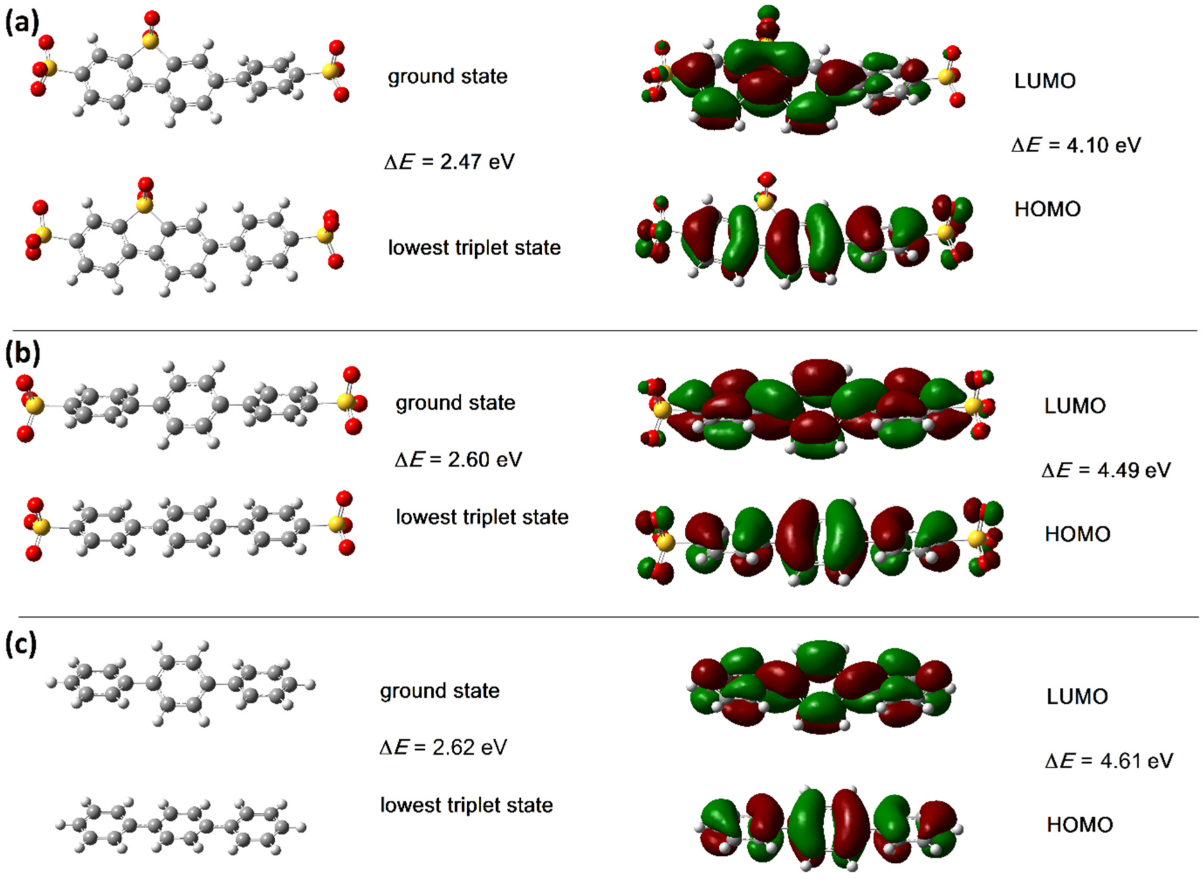

Fig. S 8 Left: Optimized structures of the ground states as well as the lowest triplet states of **SO_2TDS** (a), TDS (b) and *p*-terphenyl (c) at the B3LYP/6-31+G(d,p) level of theory and the solvation model IEFPCM for water, together with their corresponding energy differences. Right: Frontier orbitals of the ground states using the same computational method. See text for details.

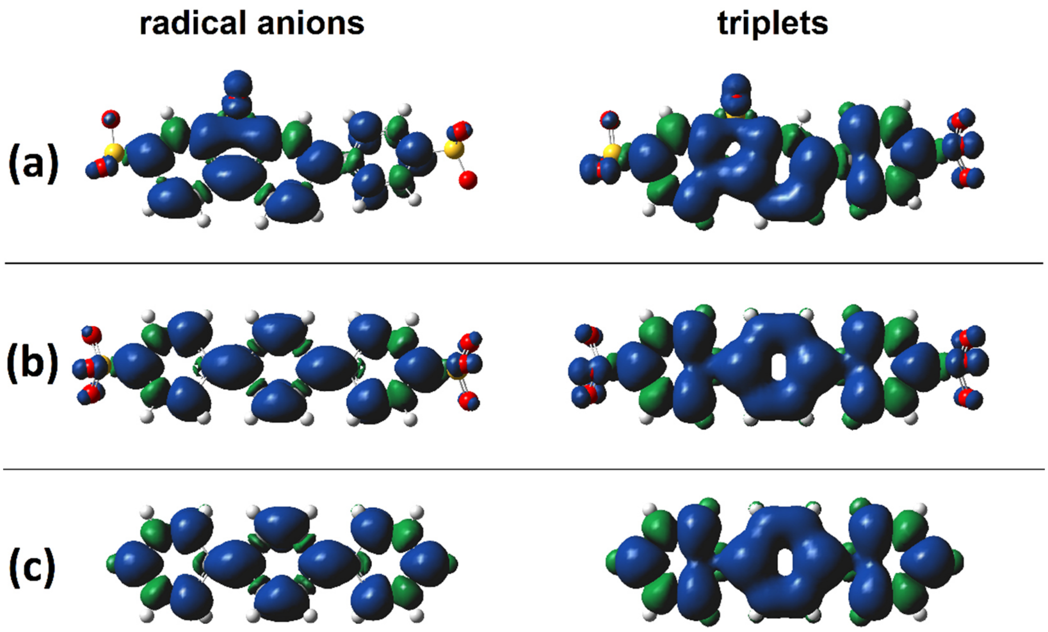

Fig. S 9 Computed spin densities (B3LYP/6-31+G(d,p), solvation model IEFPCM for water) for the optimized radical anion (left) and triplet (right) structures of **SO_2TDS** (a), TDS (b) and *p*-terphenyl (c). Blue color represents positive spin densities, whereas green represents negative spin densities. See text for details.

5 Energetic considerations

The energies of the **excited singlet states** were determined experimentally from the intersections of the absorption and fluorescence spectra of the respective terphenyl derivatives (Table 1 of the main paper). The predicted energies from DFT calculations (compare, Table S 2 in Section 4) are too high by about 0.2 eV, but they clearly support the experimentally observed trends. In principle, the triplet energies can be extracted from low-temperature emission spectra, but the low ISC quantum yield of TDS and the poor glass formation ability of water hamper such triplet energy determinations.

To obtain the **triplet energy** (E_T) of our catalyst **SO_2TDS**, we took the DFT calculated E_T (2.47 eV) and considered the results of our quenching experiments with well-characterized energy acceptors. Dexter energy transfer (TTET) reactions can proceed with diffusion-controlled kinetics for E_T(donor)>E_T(acceptor), or they can proceed in an activation-controlled fashion with rate constants significantly below the diffusion limit.[31] From the quenching with NDS (E_T(NDS) = 2.58 eV)[32] as acceptor we determined a rate constant for the energy transfer three orders of magnitude below the diffusion limit (see Section 2.3) indicating an "uphill" energy transfer, which is endergonic by 0.11 eV based on our DTF calculations. The relation between the triplet energy difference and the (uphill) Dexter energy transfer kinetics is well established.[19,33] Assuming 1 × 10^9 $M^{-1}s^{-1}$ as the diffusion rate constant for the reaction between two dianionic species in our reaction medium and the above-mentioned ΔE_T (0.11 eV), an energy transfer rate of 1.1 × 10^7 $M^{-1}s^{-1}$ can be calculated, which is very close to the experimental value (7.3 × 10^6 $M^{-1}s^{-1}$).

Moreover, the LFP quenching studies with F-Cin also confirm the E_T(**SO_2TDS**) obtained from DFT calculations. The triplet energy of F-Cin is on the order of 2.4 eV.[3,34] Hence, the energy transfer from **$^3SO_2$TDS** to F-Cin is exergonic by about 0.1 eV, and we indeed observed diffusion-controlled energy transfer kinetics (see Section 2.4). All these experimental results strongly support the calculated E_T(**SO_2TDS**) = 2.47 eV, and this value was used for an estimation of the **SO_2TDS** reduction potential, as described in the next paragraphs.

The **redox potential** for the reduction of **SO_2TDS** was not measured directly due to the difficulties associated with (reductive) cyclic voltammetry in water. However, we estimated that quantity using a comparative method. We rely on studies concerning the Rehm-Weller equation, which describes the relation between the energetics of a photoinduced electron transfer reaction and the corresponding rate constant.[35,36] Our LFP investigations gave a k_{ET} for the reduction of **$^3SO_2$TDS** with HAsc⁻ of about 1×10^9 $M^{-1}s^{-1}$ (see Section 3.1). The reductive quenching of singlet-excited **SO_2TDS** by HAsc⁻ (Fig. S 1), which has to be strongly exergonic owing to the high singlet-state energy of **SO_2TDS**, is more than twice as fast and we regard that value (2.2×10^9 $M^{-1}s^{-1}$) as the diffusion limit for a reaction between a dianionic compound and a monoanionic quencher.[12,37]

Electron transfer reactions with rate constants slightly below the diffusion limit, as measured for the reduction of **$^3SO_2$TDS**, usually have a driving force approaching zero, i.e. $\Delta G \sim 0$ eV.[35,38,39] This Gibbs energy for photoinduced electron transfer reactions (with triplet-excited states) is composed of four energies/potentials of the reactants and described by the following formula:[6,35]

$$\Delta G = E_{1/2}(D) - E_{1/2}(A) - E_T(A) + E_{Coul}$$

(Eqn. 4)

With ΔG as the Gibbs energy, $E_{1/2}$ as the redox potential of the electron donor (D, HAsc⁻) or acceptor (A, **SO_2TDS**), the triplet energy of the acceptor $E_T(A)$ as well as a coulomb term E_{Coul} (which is very close to zero due to the involvement of the uncharged $HAsc^\bullet$ and the highly polar solvent water).[3,16] With the previous assumption of $\Delta G = 0$ eV, E_T(**SO_2TDS**) = 2.47 eV, $E_{1/2}$ ($HAsc^-/HAsc^\bullet$) = 0.72 V vs. NHE[40] and after rearranging **(Eqn. *4)***, the reduction potential of **SO_2TDS** can be estimated: it amounts to −1.75 V vs NHE. This estimation does only depend on a redox potential of a well-investigated reference system (ascorbate in water), excited-state energies and rate constants that have been directly measured in water. We, therefore, regard our comparative procedure as more reliable than measuring the presumably highly solvent dependent reduction potential of **SO_2TDS** in an organic solvent.

Interestingly, the SOMO of the *p*-terphenyl radical anion (redox potential, –2.39 V vs. NHE)[41] is higher in energy than that of **$SO_2TDS^{\bullet-}$** by about 0.7 V. The relative SOMO energies of radical anions should reflect their electron donating abilities. Given that, these DFT-calculated properties of the radical anions support the redox potential estimations. The latter predict **$SO_2TDS^{\bullet-}$** to be less reactive by 0.64 V compared to the *p*-terphenyl radical anion, as presented above. This reactivity difference seems reasonable considering the electron-withdrawing effects of the sulfur-containing groups in **SO_2TDS**.

6 Irradiation experiments

6.1 Experimental setup

All irradiation experiments were performed under inert atmosphere, either in sealed NMR tubes (solvent D_2O) or in substance vials under Ar atmosphere (solvent H_2O). The quantitative analyses of the NMR spectra for the irradiation experiments were carried out by adding well-defined amounts of reference compounds (sodium chloroacetate, trifluoroacetic acid or potassium acetate). Some of the products formed throughout the irradiation experiments are more hydrophobic than the starting compounds and precipitated in our system, thereby hampering a reliable analysis. To avoid solubility-related errors in the NMR analysis originating from such precipitations, several reactions were performed using micelle-forming surfactants (SDS or DTAC). The characteristic NMR signals of the *cis* isomers formed during the isomerization reactions (Section 6.5) allowed straightforward product identification and quantification. The identification of the desired pinacol products (Section

6.4) as well as the differentiation between pinacol and monomeric alcohol was carried out with reference spectra from the literature[4,38,42] or with authentic reference substances. Details concerning our photoirradiation setup and product analyses are given below.

Preparation of sealed substance vials (Fig. S 10 a)): The reaction mixtures (substrate, 50 mM phosphate buffer, reference compound, DTAC if necessary, **SO_2TDS**) were dissolved in H_2O (3.0 - 4.0 mL), purged with Ar for 3 min within a substance vial, which was sealed using a septum cap. Throughout the irradiation, the vials were connected to the Schlenk line and kept under a constant Ar pressure. The vials were kept in a water bath to ensure ambient temperature, stirred with a magnetic stirrer, and placed closely to the LED. For the NMR measurements, small samples of the reaction mixture were removed and 10 vol. % D_2O (with TFA as reference for ^{19}F NMR measurements) were added.

Preparation of sealed NMR tubes (Fig. S 10 b)): The reaction mixtures (substrate, 50 mM phosphate buffer, reference compound, additives such as DTAC or SDS) were dissolved in D_2O (2.5 mL). The resulting solution was used to prepare two septum-sealed Schlenk flasks (1.0 mL), and **SO_2TDS** was added to one of them. The reaction mixtures were degassed by two freeze-pump-thaw cycles using Ar as inert gas, liquid N_2 for cooling and Schlenk line vacuum (down to 0.5 mbar). Under a flow of Ar gas, NaHAsc was added and after a final freeze-pump-thaw cycle, the Schlenk flask was set under an Ar atmosphere. The NMR tubes were evacuated and flushed with Ar three times. An aliquot of the reaction mixture (0.5 mL) was transferred into the prepared NMR tubes, which then were sealed either with a septum cap or melted off after oxygen removal. To maintain the Ar atmosphere throughout the reaction time, the septum-sealed NMR tubes were connected to the Schlenk line and kept under a constant Ar pressure. During the NMR measurements, the tubes had to be disconnected from the Schlenk line for a short time (max. 20 min). Overnight irradiation experiments were carried out with an Ar gas reservoir to maintain the inert atmosphere. Two NMR tubes were placed in a water bath closely to the LED during photoirradiation, as displayed in Fig. S 10 b).

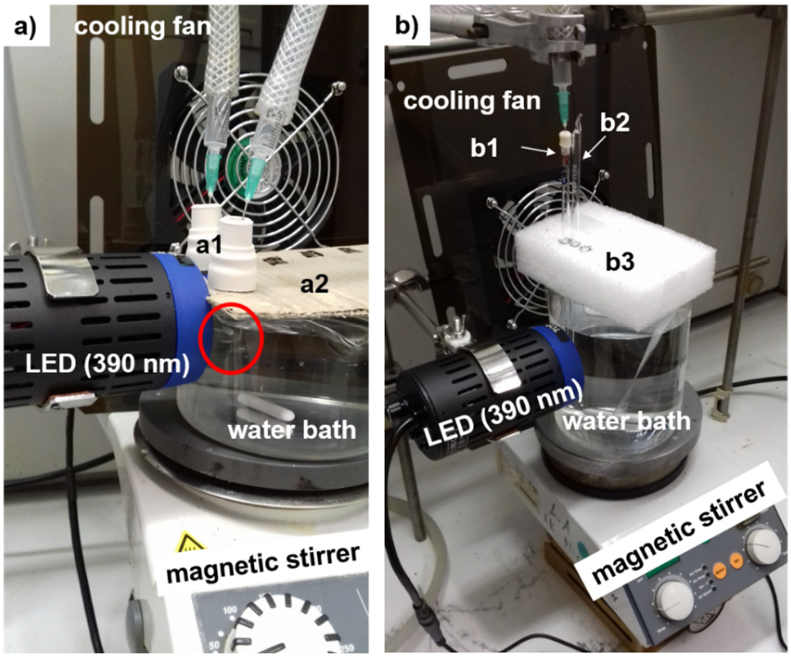

Fig. S 10 Experimental setup for the photoreactions performed in substance vials a) or in NMR tubes b). The samples were placed in custom-made holders (**a2** or **b3**) in front of the 390 nm (or 370 nm) LED. The water bath provided ambient temperature and for longer reaction times (> 2h) the cooling fan was used in addition. a) Substance vials sealed with a septum cap (**a1**) and equipped with a stirring bar (red circle). The vials have been connected to a Schlenk line (Ar). b) NMR tubes sealed with a septum cap and connected to a Schlenk line (**b1**) or flame-sealed under vacuum (**b2**).

6.2 Additional UV-Vis spectra

The following three figures display the absorption spectra of the compounds used for the NMR-scale reactions, pinacol coupling or dechlorination (Fig. S 11) and isomerization reactions (Fig. S 12), as well as the compounds relevant for optical spectroscopy (Fig. S 13). The buffer systems/concentrations were chosen to resemble the respective conditions of the sample reactions or LFP measurements. All compounds are fully transparent in the emission range of the 390 nm LED used for photocatalysis and at 355 nm, the excitation wavelength for LFP experiments. The only exception is the ascorbate dianion (Fig. S 13) with a very low molar absorption coefficient at 355 nm,[15] which was therefore used in low concentrations (for further explanations, see Section 3 and Fig. S 6).

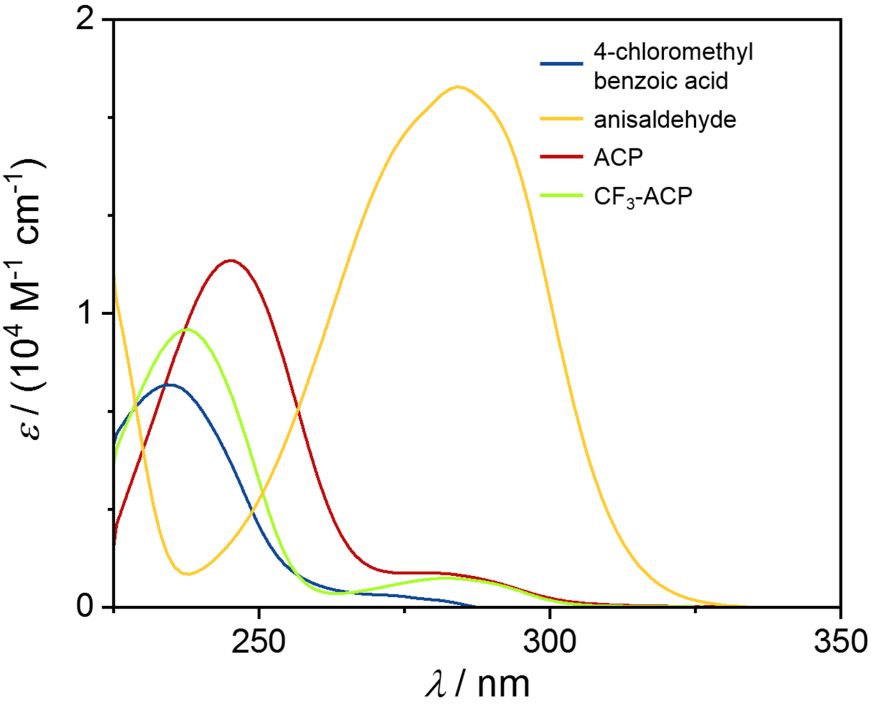

Fig. S 11 Absorption spectra of the carbonyl compounds for the pinacol coupling reactions, measured in 50 mM phosphate buffer (pH 7.2) and the substrate used for the dechlorination, measured in 10 mM Na_2HPO_4.

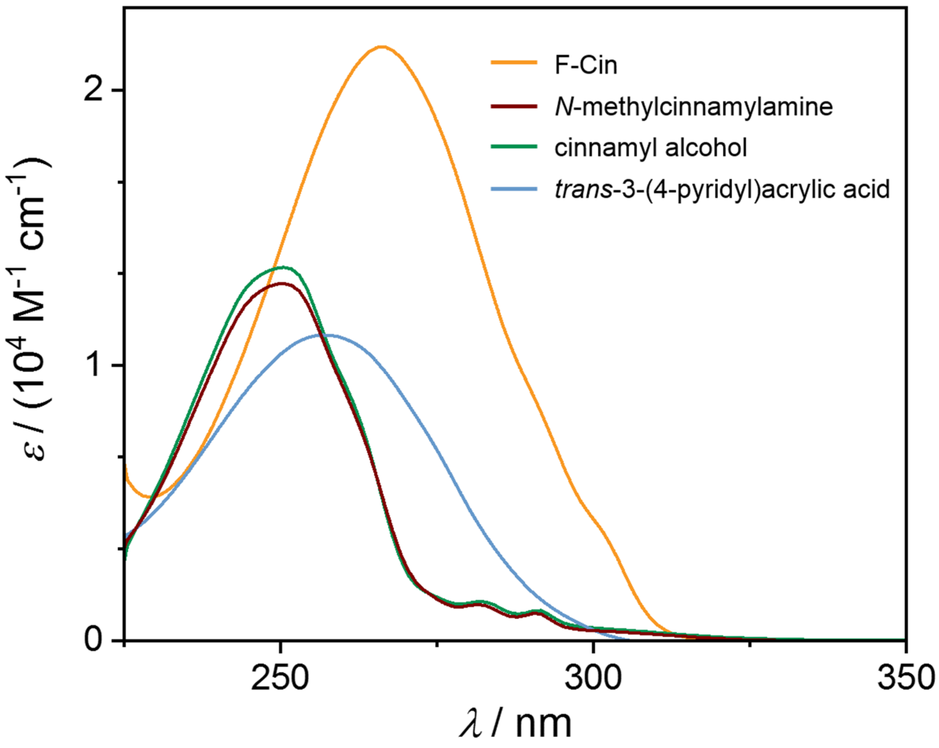

Fig. S 12 Absorption spectra of the substrates used for the isomerization reactions (F-Cin and cinnamyl alcohol in 50 mM phosphate buffer at pH 7.2; *N*-methylcinnamylamine in 10 mM NaH_2PO_4; *trans*-3-(pyridyl)acrylic acid in 10 mM Na_2HPO_4).

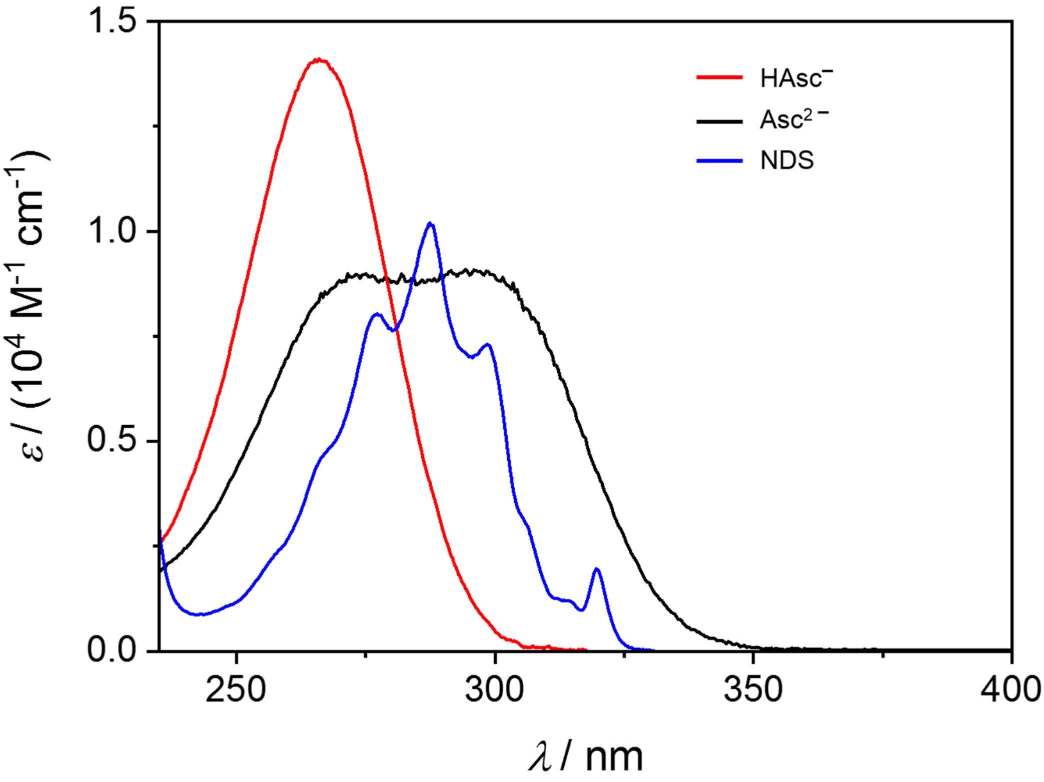

Fig. S 13 Absorption spectra of NDS, ascorbate monoanion (pH 7.6) and dianion (pH 12.7).

6.3 Interactions with DTAC and SDS micelles

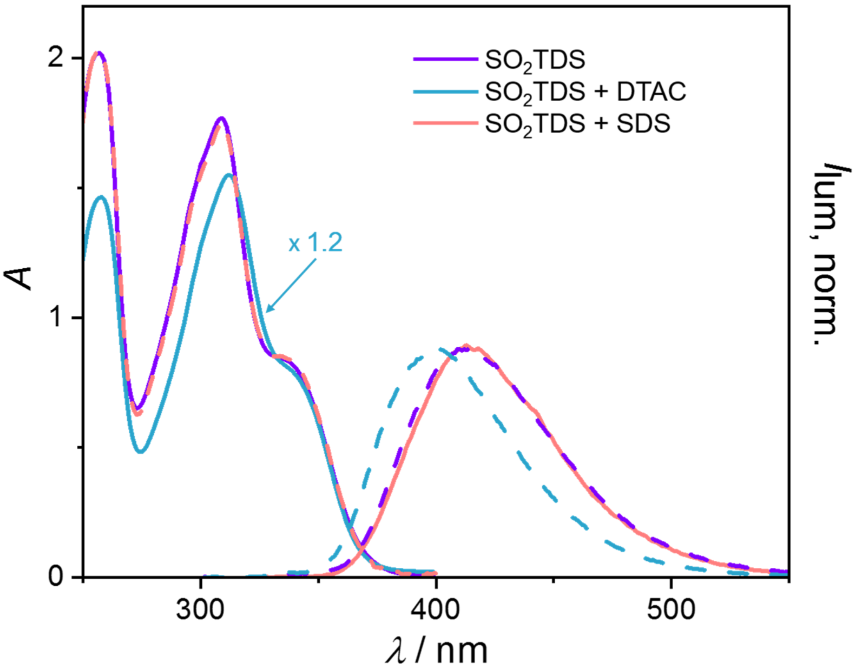

Fig. S 14 Comparison of absorption and emission spectra of aqueous solutions containing **SO_2TDS** (80 μM) in neat water (purple), with DTAC (48 mM, turquois) and with SDS (25 mM, pink). The absorption and emission spectra have been scaled such that the long wavelength absorption bands and the emission bands are at the same intensity.

Both absorption and emission spectra of **SO_2TDS** in the presence of DTAC employed at concentrations well above its critical micelle concentration[43] show pronounced changes as compared to the spectra in neat water (Fig. S 14). Specifically, the emission spectrum is blue-shifted in the presence of cationic DTAC micelles and the main UV absorption bands are less intense. Moreover, the fluorescence lifetime of singlet-excited **SO_2TDS** decreases significantly from 5.2 ns to 3.3 ns upon DTAC addition.

These effects clearly indicate an interaction between the catalyst molecules and DTAC micelles. We speculate that the **SO_2TDS** molecules are located in close proximity to the cationic head groups as a result of Coulombic attraction. In the case of anionic SDS micelles, absorption and emission spectra remained unmodified, and interactions with **SO_2TDS** as observed for DTAC micelles are less likely. This can be explained by the Coulombic repulsion between the negatively charged head groups of the SDS molecules/micelles and the doubly negatively charged **SO_2TDS**. Micelles in solution are not a static construct but are in a dynamic equilibrium with their environment. Consequently, all molecules in a micellar solution take part in this equilibrium and micelles can act as a dynamic reservoir for catalyst molecules, substrates or products. For the electron transfer reactions (pinacol coupling with CF_3-ACP) with a microheterogeneous environment of SDS micelles, this effect has proven useful.

The concentration of micelles in solution was estimated using the following equation ([mic]…concentration of micelles, [surfactant]…weight-in concentration of either SDS or DTAC, cmc…critical micelle concentration, $\mathrm{N_{agg}}$…aggregation number):[43]

$$[\text{mic}] = \frac{[\text{surfactant}] - \text{cmc}}{N_{agg}}$$

(Eqn. 5)

The values for cmc (cmc(DTAC) = 22 mM, cmc(SDS) = 8 mM) and $\mathrm{N_{agg}}$ ($\mathrm{N_{agg}}$(DTAC) = 60, $\mathrm{N_{agg}}$(SDS) = 60) were taken from ref.[43].

6.4 Additional data and details for pinacol coupling reactions

Acetophenone (ACP)

Most results of the pinacol coupling with ACP as starting material are discussed in the main paper. Control experiments confirm that the entire catalytic system is required for the reaction to occur successfully. Besides the reaction scheme and selected ^{1}H NMR spectra (for all control experiments, see Fig. 3 of the main paper), Fig. S 15 shows a plot with the temporal evolution of the ^{1}H NMR signals of the product (blue) and consumption of the starting material (red) during photoirradiation, together with a fit curve to guide the eye. For this analysis, we used the integrated methyl ^{1}H NMR peaks corresponding to ACP and the *dl*/meso forms of the product (same color code for all parts of Fig. S 15). The plot does not show a lag phase, which can be seen in the region below 5 h. This observation indicates a direct reaction of **SO_2TDS**$^{\bullet-}$ with ACP (and not with catalyst-derived decomposition products) and thus provides additional evidence for the proposed reaction mechanism (see main paper and Section 3.2).

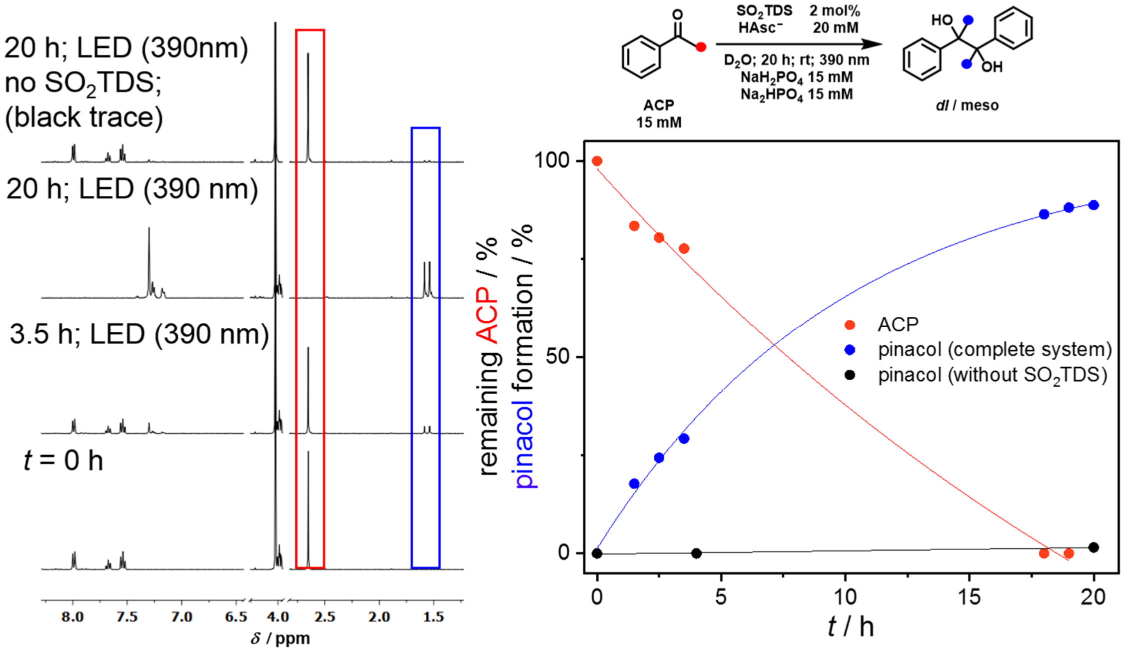

Fig. S 15 Additional experiments on the pinacol coupling reaction of ACP. The reaction scheme includes the pertinent conditions. The time-dependent conversion of the ACP (red trace) and the formation of the pinacol product (blue trace) was obtained from quantitative NMR experiments by analyzing the color-coded methyl signals. The black data set corresponds to the control experiment, which was irradiated under the same reaction conditions, but lacking **SO_2TDS** and yields practically no pinacol product. For further information, see main paper and text.

Anisaldehyde

This substrate was chosen because of the electron-donating effect of the methoxy substituent, which makes the one-electron reduction of the carbonyl group more difficult. Without the supramolecular environment, only traces of the desired pinacol were observed after 12 h of irradiation, as well as partial precipitation of the product. The consumption of anisaldehyde in this irradiation experiment (without DTAC micelles) is almost 50 % after 12 h, but side product formation and only about 2% of the pinacol were observed (NMR spectrum 1, signals in the blue frame in Fig. S 16). Also, the signals of the pinacol product and the reduced alcohol overlap. Related experiments (higher catalyst loading) with DTAC micelles resulted in a high yield of the pinacol after 18 h of irradiation.

The table in Fig. S 16 lists our reaction conditions. The ascorbate concentrations were increased at higher catalyst loadings. It is worth mentioning that all end-point NMR spectra still showed signals corresponding to the ascorbate (not shown here). We conclude that for all reactions this compound was added in excess and therefore it is unlikely that different ascorbate concentrations are responsible for the observed results.

The ^{1}H NMR spectra of the irradiation experiment without DTAC showed several overlapping peaks of different intensities (Fig. S 16, spectrum 1, product mixture [a]). The comparison to spectra from literature allowed us to identify the two main products. The two most intense doublets of similar intensity in the aromatic region correspond to the reduced alcohol (4-methoxybenzylalcohol),[42] which is an undesired side product in our case. The second compound is the desired pinacol product,[38] which is formed as *dl/*meso mixture. As expected, four doublets can be seen in the corresponding ^{1}H NMR spectrum, out of which three are overlapping with the starting material or the reduced (monomeric) alcohol. This irradiation experiment resulted in a conversion of 44 % (Fig. S 16, table, entry 1), which slightly differs from the yield of detected (side) products. An explanation for this effect is provided by the decreased water solubility of the pinacol product, which resulted in precipitation in the NMR tube.

To confirm the pinacol formation for the reactions with DTAC micelles (and to exclude alcohol formation), a ^{1}H NMR spectrum (not shown) of the reduced alcohol was recorded under the corresponding reaction conditions. The additional signals so obtained did not overlap with those of the successful pinacol reactions (Fig. S 16, spectra 2 and 3) but they did show the expected signals (two doublets with identical intensities) of the reduced (monomeric) alcohol. We, therefore, conclude that the micellar approach is indeed useful for increasing the selectivity for pinacol formation.

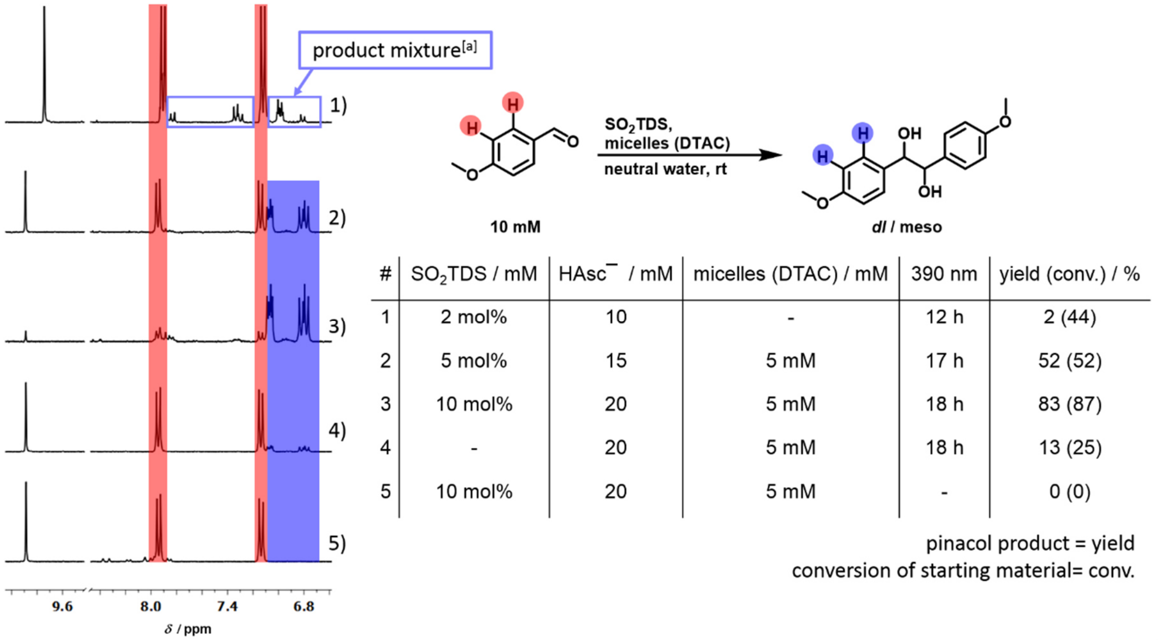

#	SO_2TDS / mM	HAsc⁻ / mM	micelles (DTAC) / mM	390 nm	yield (conv.) / %
1	2 mol%	10	-	12 h	2 (44)
2	5 mol%	15	5 mM	17 h	52 (52)
3	10 mol%	20	5 mM	18 h	83 (87)
4	-	20	5 mM	18 h	13 (25)
5	10 mol%	20	5 mM	-	0 (0)

pinacol product = yield
conversion of starting material= conv.

Fig. S 16 Pinacol coupling of anisaldehyde. The reaction scheme contains general experimental conditions and the structure of the (diastereomeric) pinacol product. The table below lists all (control) experiments performed and the corresponding ^{1}H NMR spectra show conversion / product formation under the respective reaction conditions. For the quantitative NMR analysis, the aromatic protons were used (same color code as in the reaction scheme). Entry 1 corresponds to the irradiation without the micellar environment, which also explains the shifted signals in the ^{1}H NMR spectrum. [a] For further information, see text.

4-(Trifluoromethyl)acetophenone (CF_3-ACP)

Exact conditions of the pinacol coupling of CF_3-ACP and corresponding control experiments are given in the reaction scheme and in the table presented in Fig. S 17. The irradiation experiments without microheterogeneous environment were performed in non-deuterated water using ^{19}F NMR spectroscopy for the quantitative analysis (see Section 6.1 for details). Owing to the broad water signal, the corresponding ^{1}H NMR spectra were not used for the evaluation of the reaction outcome. Full conversion was observed (^{19}F NMR) after 5 h of irradiation, but merely half of the expected integrals were found in the product peaks (spectra 3) and 4)). We ascribe this effect, combined with the turbidity of the solution, to the low solubility of the pinacol product. To improve the solubility of the reaction product for a reliable quantification, we performed additional experiments with SDS micelles in the reaction mixture (see main paper). The irradiation experiments with SDS micelles were performed in D_2O and quantified using the ^{1}H NMR spectra (spectra 1) and 2)). To verify the success of the coupling reaction, we added the reduced alcohol (1-(4-(trifluoromethyl)phenyl)ethanol) into the NMR tube containing solution 1. The corresponding ^{19}F NMR spectrum (Fig. S 17 bottom, right) shows an additional, distinct, and non-overlapping signal (a similar observation was made for ^{1}H NMR, spectra are not shown) confirming the formation of the desired pinacol product as the result of our photoreaction.

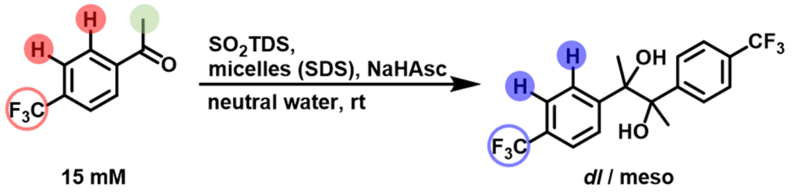

#	SO_2TDS / mM	NaHAsc / mM	micelles (SDS) / mM	390 nm	yield / %
1	2 mol%	20 mM	5 mM	4 h	85
2	2 mol%	20 mM	5 mM	-	0
3	2 mol%	20 mM	-	5 h	47
4	2 mol%	20 mM	-	-	0

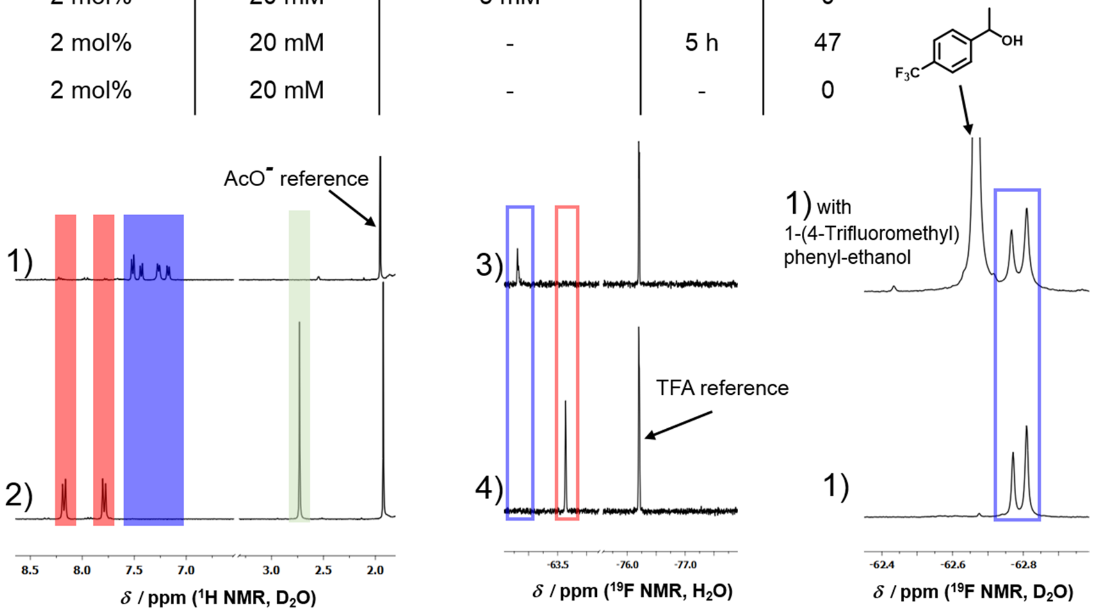

Fig. S 17 Pinacol coupling of CF_3-ACP. Reaction scheme and table with conditions of the (control) experiments as well as the desired coupling product. The corresponding NMR spectra show the signals used for the quantitative analysis with the same color code as in the scheme. NMR spectra: Left, ^{1}H NMR spectra of reactions 1) and 2) in D_2O with acetate as reference compound for quantifications. Middle, ^{19}F NMR spectra of 3) and 4) in H_2O with TFA as reference. Right, comparison of the ^{19}F NMR spectra of the pinacol product with that of the reduced monomeric alcohol (*R/S*)(1-(4-(trifluoromethyl)phenyl)ethanol). For further explanations, see text.

6.5 Additional data and details for isomerization reactions

Unless indicated otherwise, we did not observe substrate-derived side products or turbid solutions after irradiation. Hence, the NMR quantifications of the *cis*-*trans* ratios directly reflect the yields of the desired *cis* isomers.

370 nm driven isomerization of F-Cin

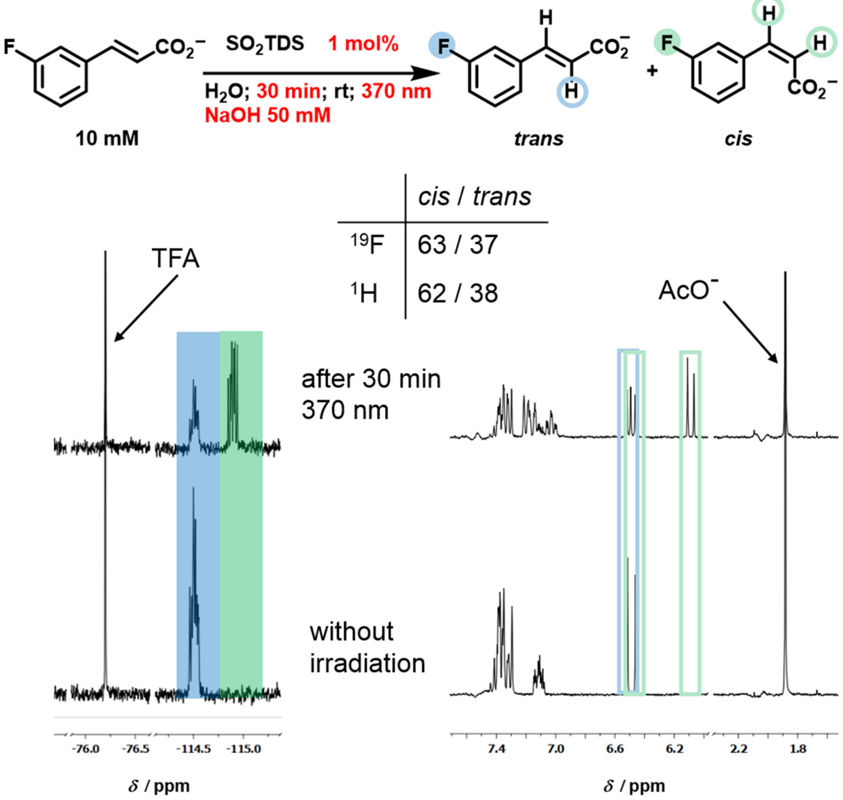

	cis / *trans*
^{19}F	63 / 37
^{1}H	62 / 38

Fig. S 18 Reaction scheme for the F-Cin isomerization reaction under 370 nm LED irradiation employing a lower catalyst loading, together with the corresponding ^{19}F and ^{1}H NMR spectra and the quantitative evaluation. The signals used for the quantitative analysis are color-coded. This reaction was performed in NaOH to improve the solubility of both substrate and product.

N-Methylcinnamylamine (protonated)

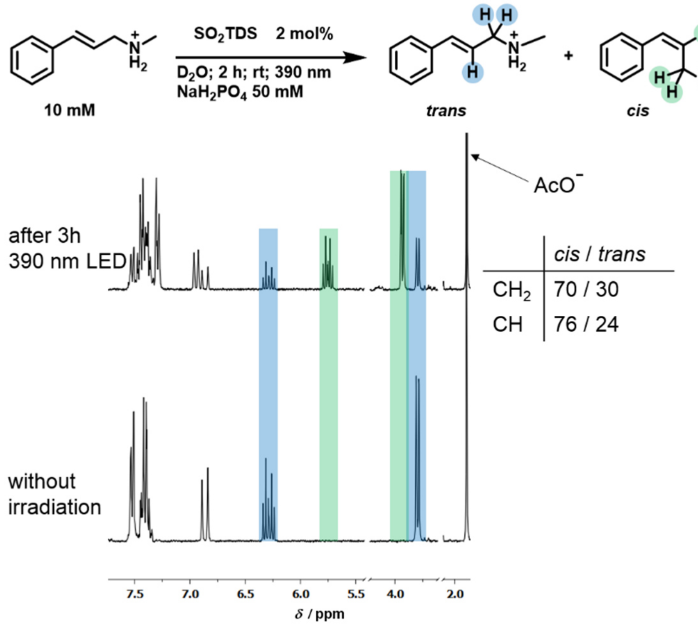

	cis / *trans*
CH_2	70 / 30
CH	76 / 24

Fig. S 19 Reaction scheme of the *N*-methylcinnamylamine isomerization, ^1H NMR spectra and the corresponding quantitative analysis. The proton signals used for the evaluation of the NMR spectra are color-coded with the corresponding product protons in the reaction scheme. The pH of the solution was adjusted to ~4 using NaH_2PO_4 in order to convert the substrate into its protonated water-soluble form.

Cinnamyl alcohol without DTAC

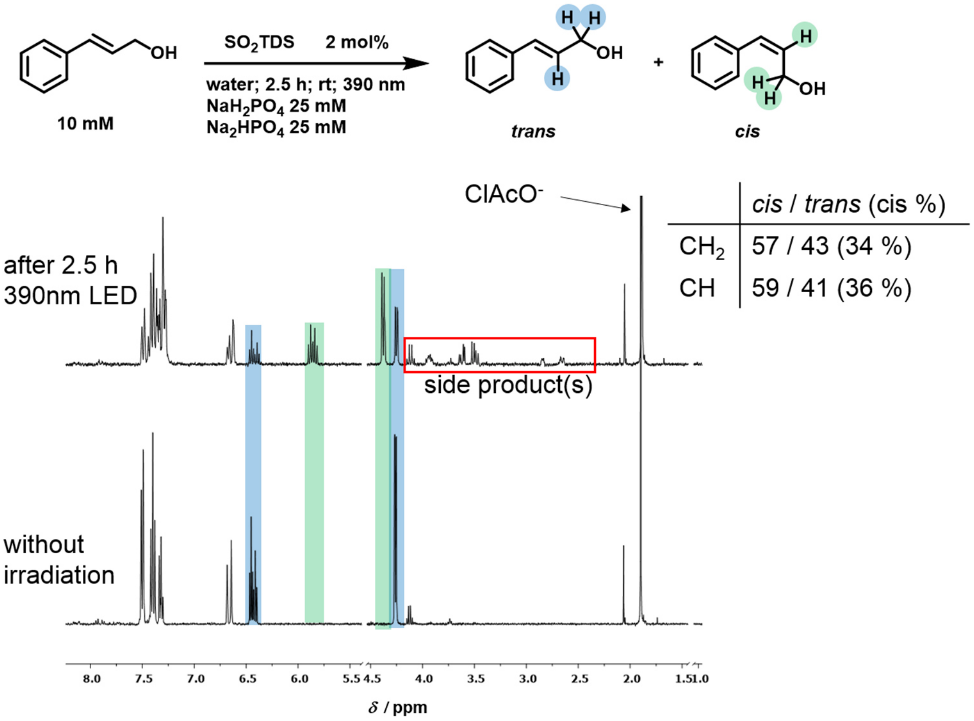

	cis / *trans* (cis %)
CH_2	57 / 43 (34 %)
CH	59 / 41 (36 %)

Fig. S 20 Reaction scheme and conditions for the isomerization reaction of cinnamyl alcohol, as well as ^1H NMR spectra and the corresponding quantitative analysis with the absolute *cis* yield given in brackets. The signals used for the quantitative evaluation are color-coded with the product protons in the reaction scheme. Highlighted with the red frame are the signals of the undesired side product(s) that formed during the reaction. The singlet next to the reference peak is an impurity in the starting material and not involved in the reaction (integral remains identical).

Cinnamyl alcohol with DTAC micelles

The addition of DTAC leads to an increase of the absolute *cis* yield of the isomerization reaction by suppressing side reactions, as the quantitative analyses of our comparative photoreactions shown in Figs. S 20 and S 21 unambiguously demonstrate.

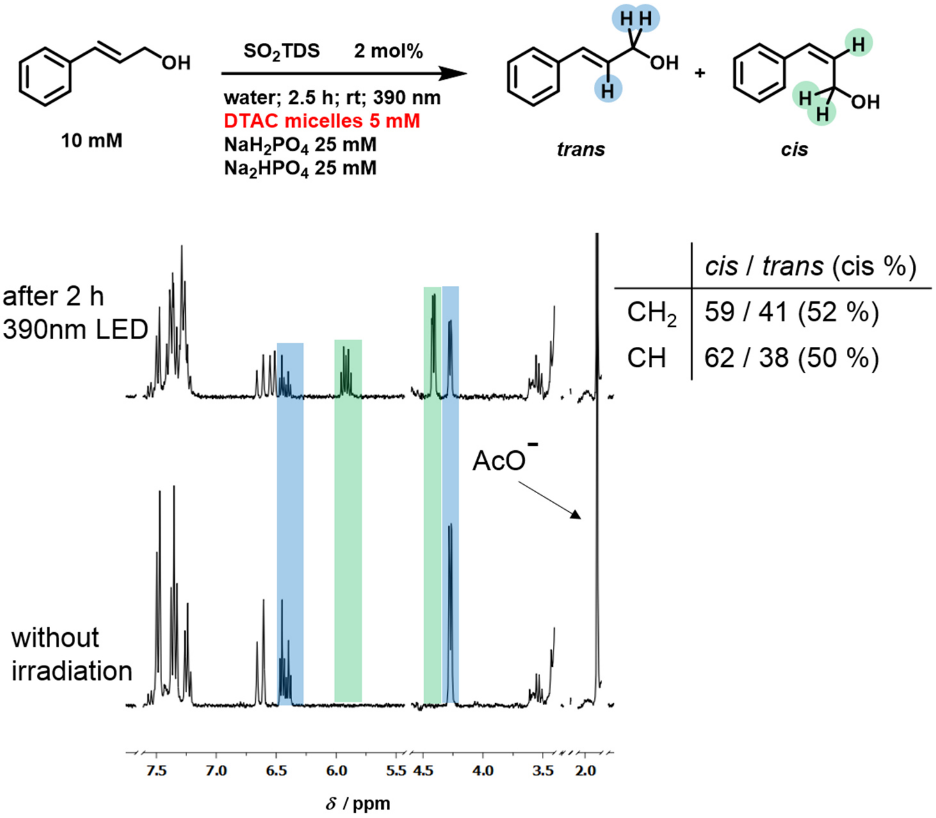

	cis / *trans* (cis %)
CH_2	59 / 41 (52 %)
CH	62 / 38 (50 %)

Fig. S 21 Reaction scheme and conditions for the cinnamyl alcohol isomerization with DTAC addition, as well as ^{1}H NMR spectra and the corresponding quantitative analysis with the absolute *cis* yield given in brackets. The signals used for the quantitative evaluation are color-coded with the product protons in the reaction scheme. The reference signal overlaps slightly with the DTAC signals, which should not affect the quantitative analysis as both species are not involved in the reaction.

6.6 Benchmark reactions for comparison of water-soluble photocatalysts

For both reaction types, electron and energy transfer, we have chosen one reference reaction to compare **SO_2TDS** with other water-soluble photocatalysts (compare, Table S 3) that are known for triplet reactivity.

For the electron transfer, a dechlorination reaction of 4-(chloromethyl)benzoic acid was investigated, yielding either the deuterated monomer or a dimeric dibenzyl-like product (left part of Fig. S 22). The NMR-based analysis of the reaction outcome and the differentiation between both products is straightforward, as described recently.[34] The sample ^{1}H NMR spectrum before the irradiation (0 h) also shows peaks corresponding to the photocatalyst Rubpy, which are marked with asterisks.

Both isomers *cis*- and *trans*-3-(4-pyridyl)acrylate show isolated signals in the ^{1}H NMR spectra and therefore all signal integrals were considered for the quantification of the *cis* isomer as reaction product (right part of Fig. S 22).

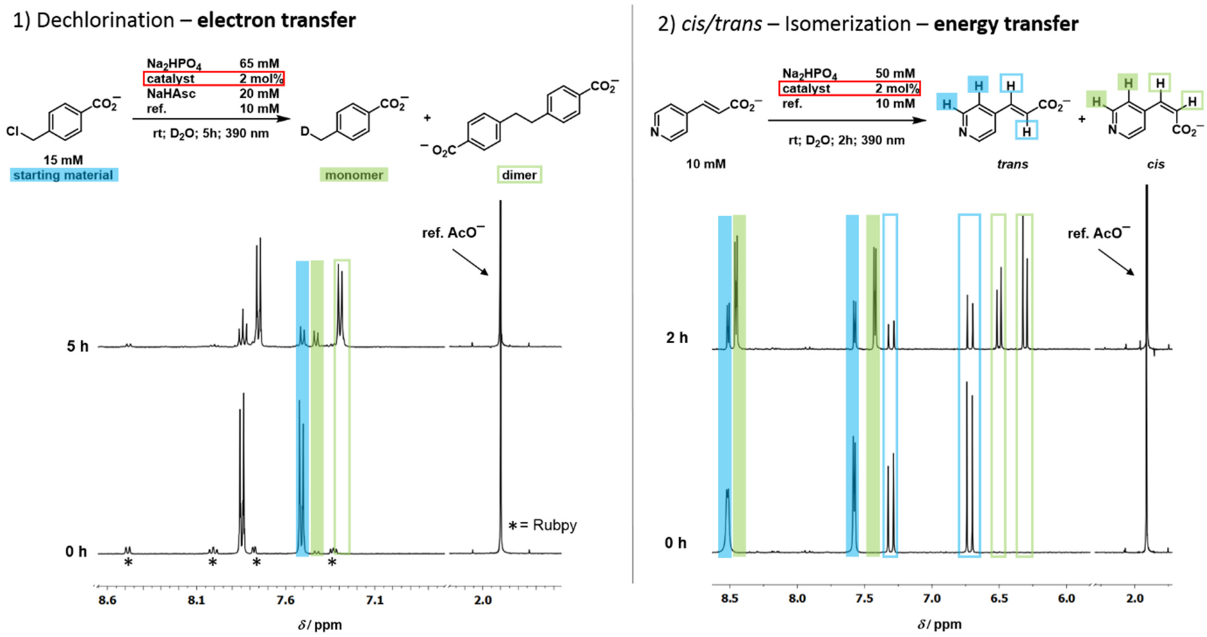

Fig. S 22 Reaction schemes including the pertinent conditions for dechlorination **1)** and isomerization **2)** reaction. Several water-soluble photocatalysts have been tested with a 2 mol% catalyst loading (red frame, for details see Table S 3). The lower part shows representative sample ^{1}H NMR spectra before (0 h) and after (electron transfer, 5h, Rubpy as catalyst; energy transfer, 2h, **SO_2TDS** as catalyst) irradiation. For both reaction types 1) and 2), the substrate signals used for quantification are highlighted in blue, whereas product signals are highlighted in green.

The results obtained for the two reactions and different catalysts are summarized in Table S 3. Under the selected sustainable reaction conditions with neutral water as solvent, and a 390 nm LED as energy source, only **SO_2TDS** is a suitable and efficient photocatalyst for both reaction types.

Table S 3 Results of the dechlorination 1) and isomerization 2) reactions (for conditions see Fig. S 22 using different water-soluble photocatalysts. Color code: >70% green; 30–70% orange; <20% red.

photocatalyst	**1) electron transfer**[b] % dichlorination (% dimer)	**2) energy transfer**[b] % *cis* isomer
Rubpy	84 (72)	16
eosinY	17 (4)	11
4-benzoylbenzoic acid	11 (3)	37
riboflavin (vit. B2)	10 (2)	81
1-pyrenecarboxylic acid[a]	47 (22)	53
-	8 (1)	5
SO_2TDS	93 (68)	71

[a] Poor solubility under the given reaction conditions, which was improved by addition of NaOD [b] Carried out with the setup shown in Fig. S 10 b).

7 NMR spectra of TDS and **SO$_2$TDS**

7.1 ^{1}H and ^{13}C NMR spectra of TDS

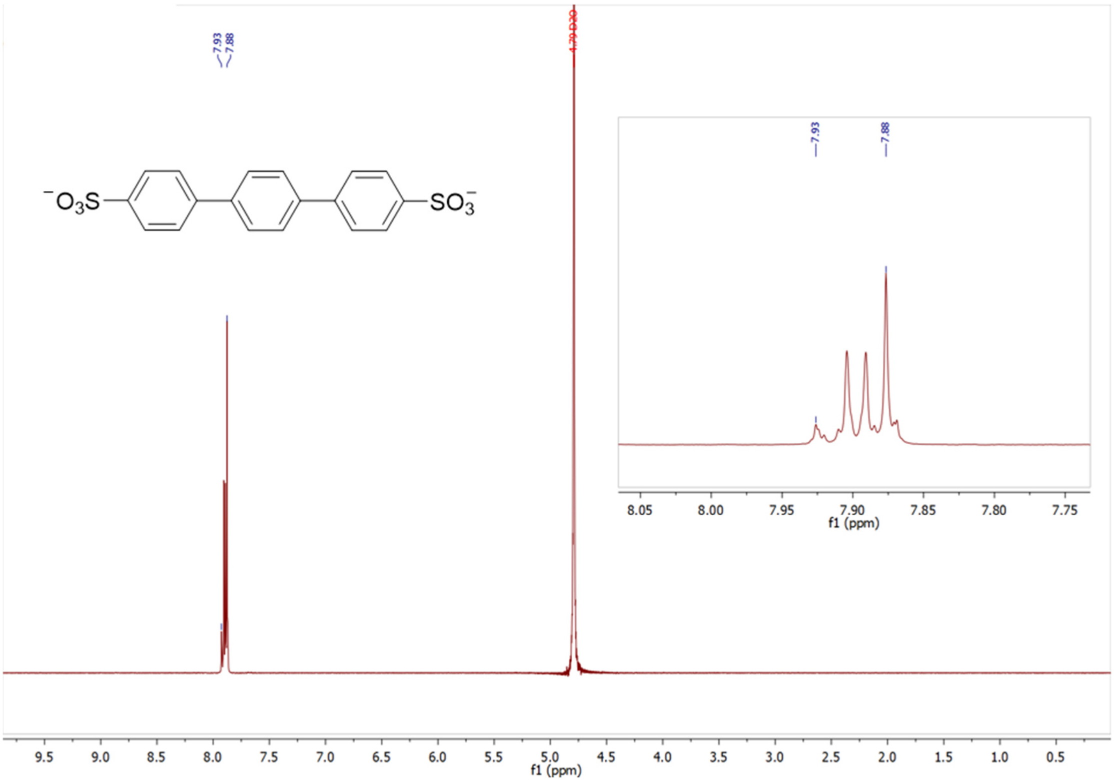

Fig. S 23 ^{1}H NMR spectrum of TDS in D$_2$O.

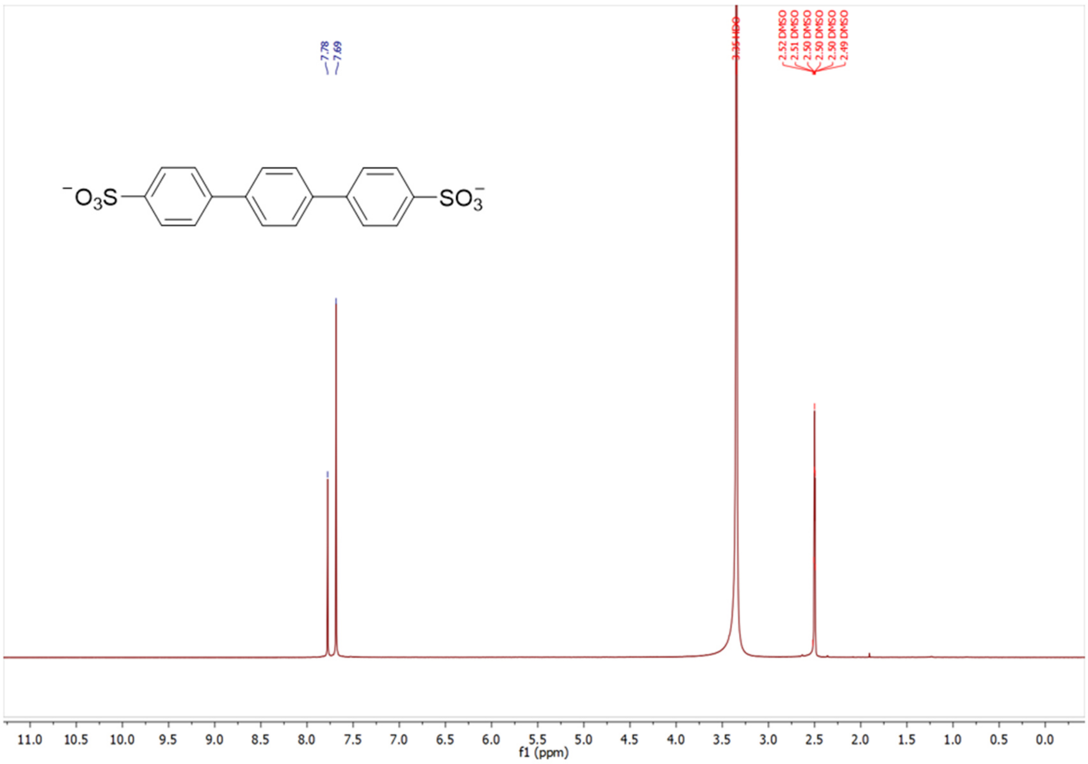

Fig. S 24 ^{1}H NMR spectrum of TDS in DMSO-*d*$_6$.

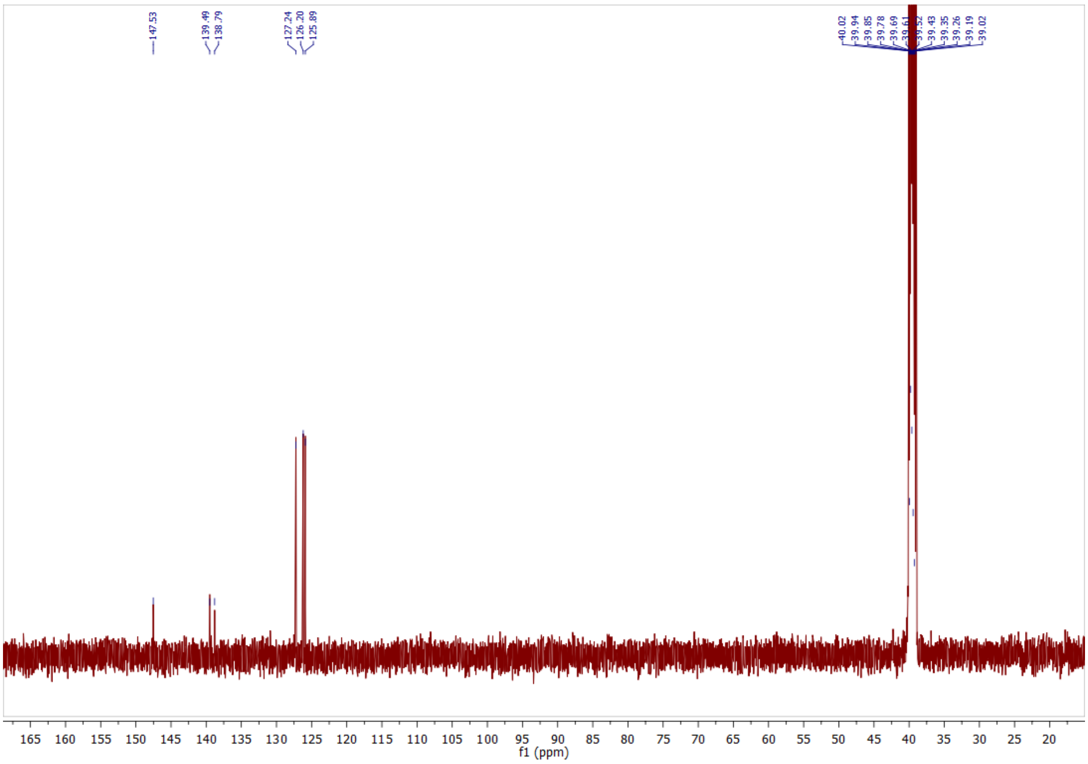

Fig. S 25 ^{13}C NMR spectrum of TDS in DMSO-d_6.

7.2 ^{1}H, ^{13}C and 2D (^{1}H, ^{13}C) NMR spectra of **SO$_2$TDS**

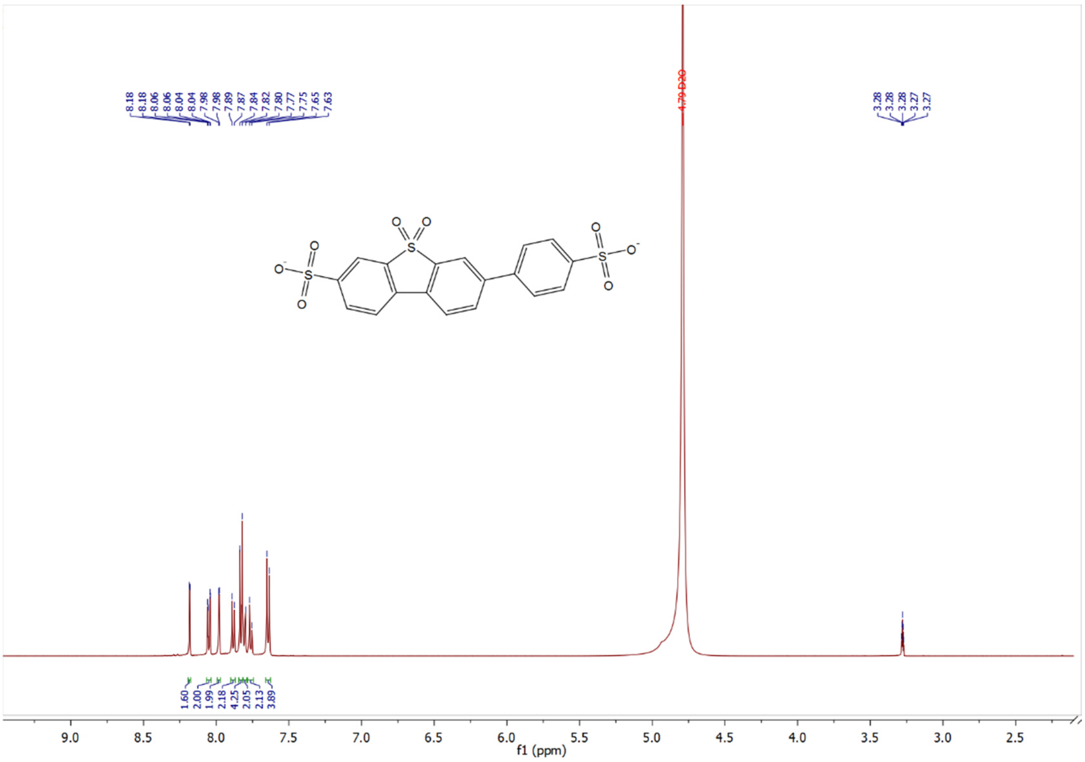

Fig. S 26 ^{1}H NMR spectrum of **SO$_2$TDS** in D$_2$O with DMSO-*d*$_6$ added as reference for ^{13}C NMR (see Figs. S 28 – S 29).

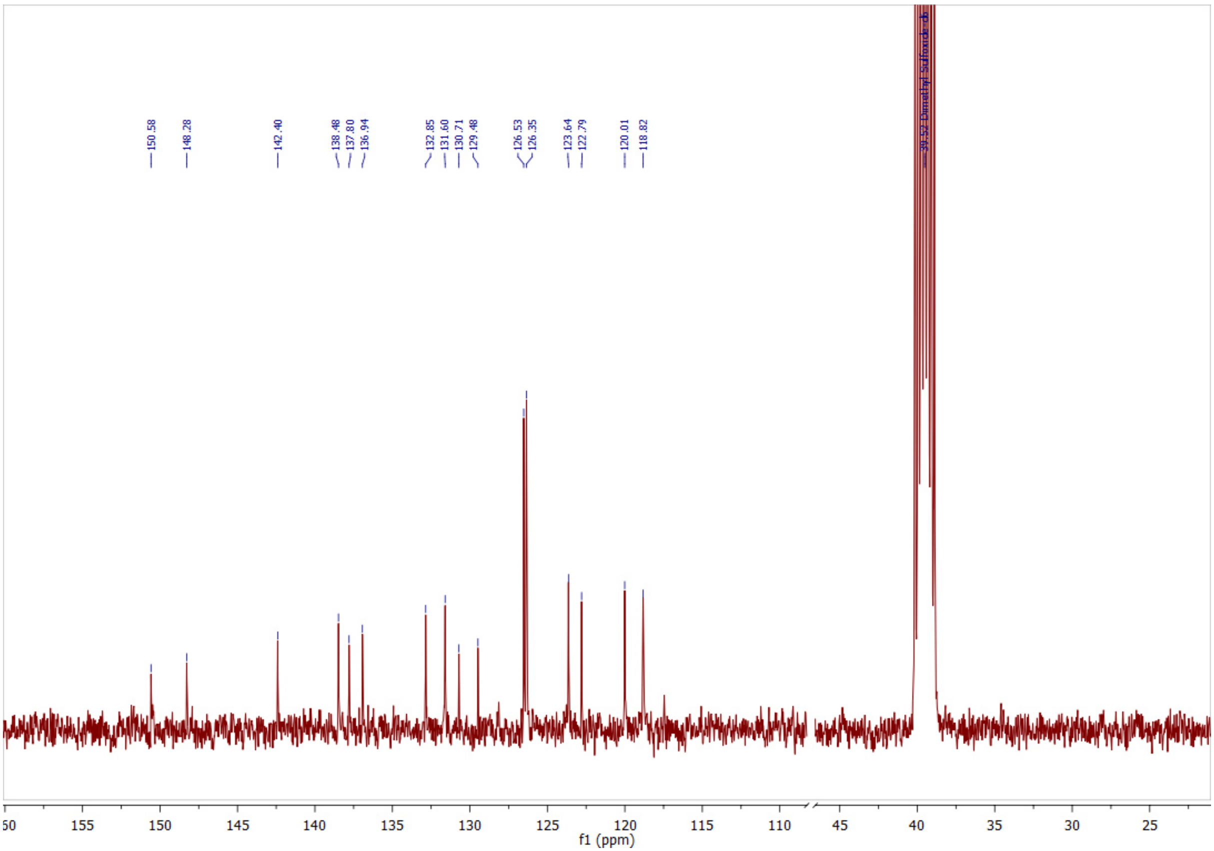

Fig. S 27 ^{13}C NMR spectrum of **SO$_2$TDS** in neat DMSO-*d*$_6$.

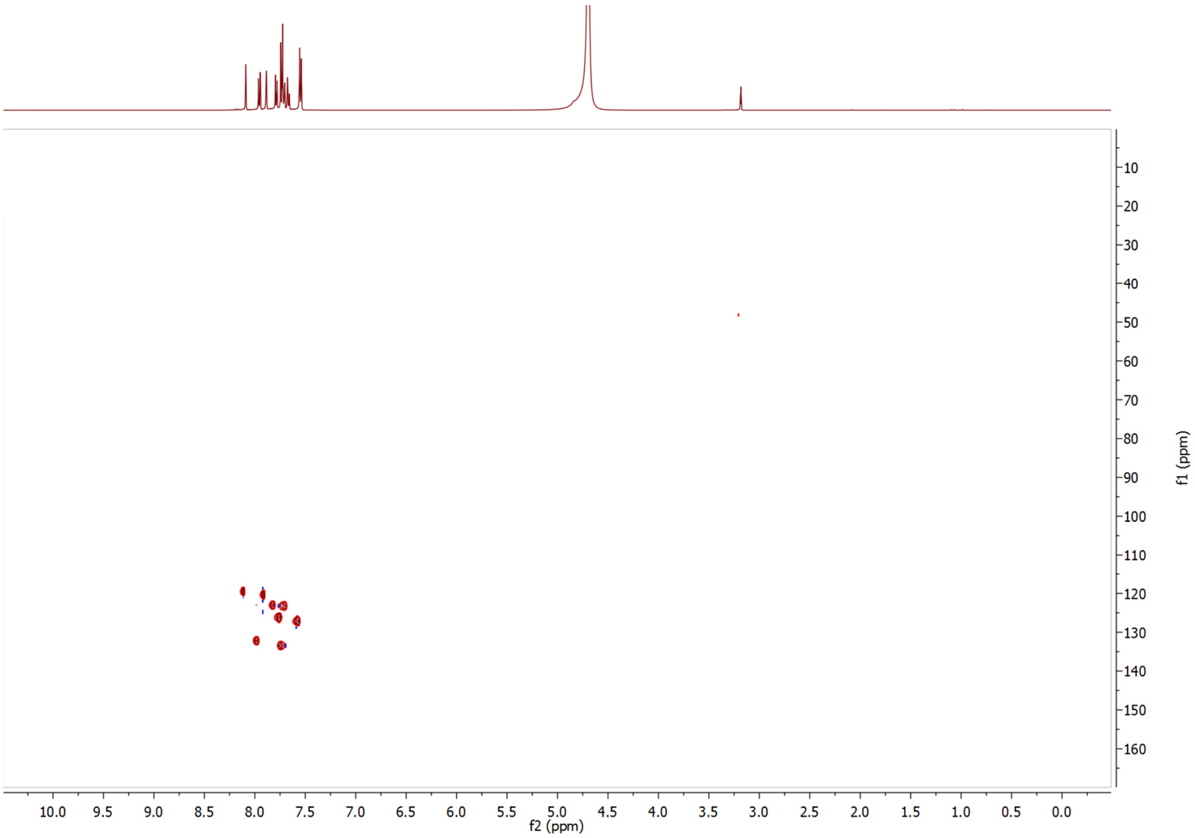

Fig. S 28 HMQC spectrum of **SO_2TDS** in D_2O with DMSO-d_6 added as reference.

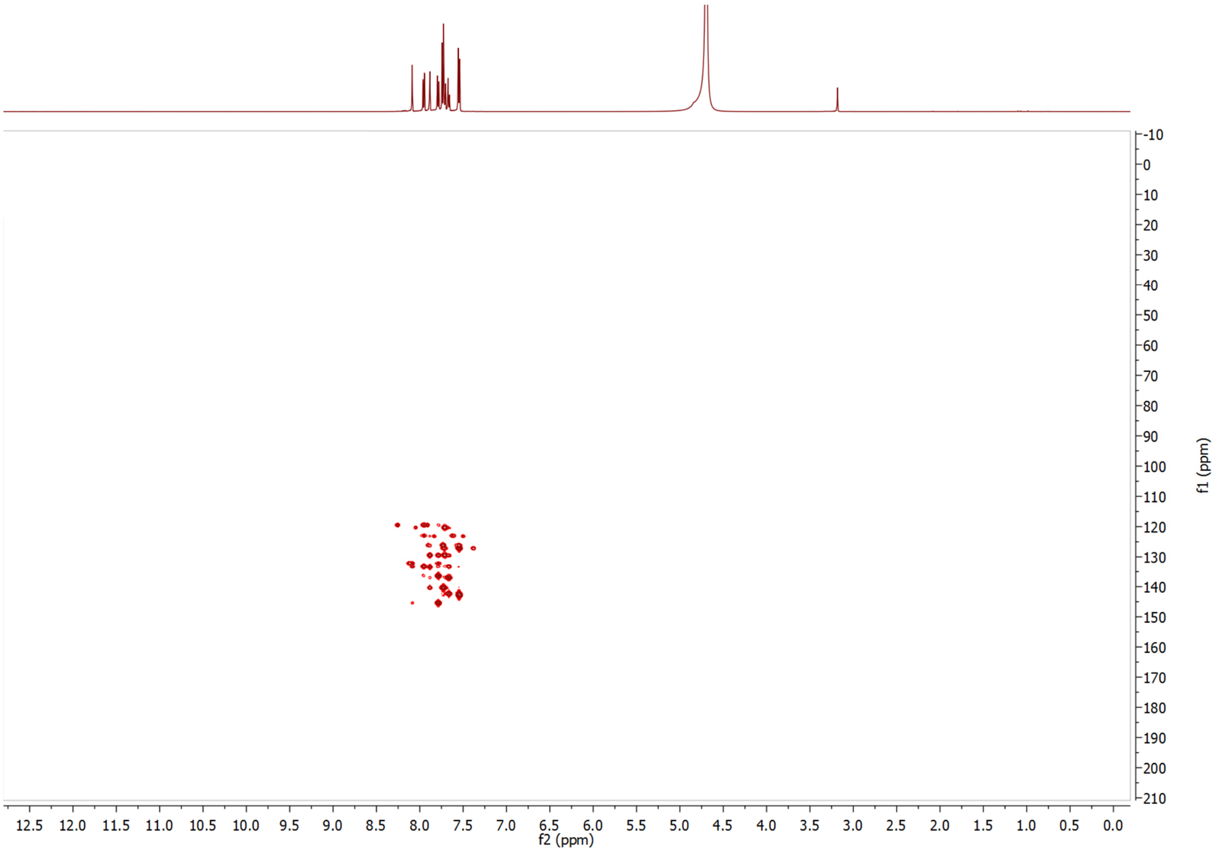

Fig. S 29 HMBC spectrum of **SO_2TDS** in D_2O with DMSO-d_6 added as reference.

8 Supplementary references

1 H. E. Gottlieb, V. Kotlyar and A. Nudelman, *J. Org. Chem.*, 1997, **62**, 7512–7515.

2 F. Zhang, M. Jiang, L.-L. Sun, F. Zheng, L. Dong, V. Shah, W.-B. Shen and Y. Ding, *Analyst*, 2015, **140**, 280–286.

3 M. Montalti, A. Credi, L. Prodi and M. T. Gandolfi, *Handbook Of Photochemistry*, 2006.

4 B. Pfund, D. M. Steffen, M. R. Schreier, M. S. Bertrams, C. Ye, K. Börjesson, O. S. Wenger and C. Kerzig, *J. Am. Chem. Soc.*, 2020, **142**, 10468–10476.

5 T. W. T. Muesmann, M. S. Wickleder and J. Christoffers, *Synthesis (Stuttg).*, 2011, **17**, 2775–2780.

6 G. J. Kavarnos and N. J. Turro, *Chem. Rev.*, 1986, **86**, 401–449.

7 N. A. Romero and D. A. Nicewicz, *Chem. Rev.*, 2016, **116**, 10075–10166.

8 S. Neumann, O. S. Wenger and C. Kerzig, *Chem. - Eur. J.*, 2021, **27**, 4115–4123.

9 G. V. Buxton, C. L. Greenstock, W. P. Helman and A. B. Ross, *J. Phys. Chem. Ref. Data*, 1988, **17**, 513–886.

10 J. N. Brønsted and C. E. Teeter, *J. Phys. Chem*, 1924, **28**, 579–587.

11 J. N. Brønsted, *Z. Phys. Chem.*, 1922, **102**, 169–207.

12 P. Debye, *Trans. Electrochem. Soc.*, 1942, **82**, 265.

13 K. Miedlar and P. K. Das, *J. Am. Chem. Soc.*, 1982, **104**, 7462–7469.

14 F. M. Hörmann, C. Kerzig, T. S. Chung, A. Bauer, O. S. Wenger and T. Bach, *Angew. Chem. Int. Ed.*, 2020, **59**, 9659–9668.

15 M. Brautzsch, C. Kerzig and M. Goez, *Green Chem.*, 2016, **18**, 4761–4771.

16 C. Kerzig and M. Goez, *Phys. Chem. Chem. Phys.*, 2014, **16**, 25342–25349.

17 M. Nemoto, H. Kokubun and M. Koizumi, *Bull. Chem. Soc. Jpn.*, 1969, **42**, 2464–2470.

18 I. Carmichael, W. P. Helman and G. L. Hug, *J. Phys. Chem. Ref. Data*, 1986, **16**, 239–260.

19 P. Klán and J. Wirz, *Photochemistry of Organic Compounds*, 2009.

20 S. Campagna, F. Puntoriero, F. Nastasi, G. Bergamini and V. Balzani, *Top. Curr. Chem.*, 2007, **280**, 117–214.

21 P. Müller and K. Brettel, *Photochem. Photobiol. Sci.*, 2012, **11**, 632–636.

22 C. Kerzig and O. S. Wenger, *Chem. Sci.*, 2018, **9**, 6670–6678.

23 S. Neumann, C. Kerzig and O. S. Wenger, *Chem. Sci.*, 2019, **10**, 5624–5633.

24 A. M. Funston, S. V Lymar, B. Saunders-Price, G. Czapski and J. R. Miller, *J. Phys. Chem. B*, 2007, **111**, 6895–6902.

25 G. E. Adams and R. L. Willson, *Faraday Trans. 1*, 1972, **69**, 719–729.

26 E. Hayon, T. Ibata, N. N. Lichtin and M. Simic, *J. Phys. Chem.*, 1972, **76**, 2072–2078.

27 M. J. Frisch, G. W. Trucks, H. B. Schlegel, G. E. Scuseria, M. A. Robb, J. R. Cheeseman, G. Scalmani, V. Barone, B. Mennucci, G. A. Petersson, H. Nakatsuji, M. Caricato, X. Li, H. P. Hratchian, A. F. Izmaylov, J. Bloino, G. Zheng, J. L. Sonnenberg,

M. Hada, M. Ehara, K. Toyota, R. Fukuda, J. Hasegawa, M. Ishida, T. Nakajima, Y. Honda, O. Kitao, H. Nakai, T. Vreven, J. Montgomery, J. A., J. E. Peralta, F. Ogliaro, M. Bearpark, J. J. Heyd, E. Brothers, K. N. Kudin, V. N. Staroverov, R. Kobayashi, J. Normand, K. Raghavachari, A. Rendell, J. C. Burant, S. S. Iyengar, J. Tomasi, M. Cossi, N. Rega, J. M. Millam, M. Klene, J. E. Knox, J. B. Cross, V. Bakken, C. Adamo, J. Jaramillo, R. Gomperts, R. E. Stratmann, O. Yazyev, A. J. Austin, R. Cammi, C. Pomelli, J. W. Ochterski, R. L. Martin, K. Morokuma, V. G. Zakrzewski, G. A. Voth, P. Salvador, J. J. Dannenberg, S. Dapprich, A. D. Daniels, Ö. Farkas, J. B. Foresman, J. V. Ortiz, J. Cioslowski and D. J. Fox, *Gaussian, Inc., Wallingford CT*, 2009.

28 T. R. Blum, Z. D. Miller, D. M. Bates, I. A. Guzei and T. P. Yoon, *Science*, 2016, **354**, 1391–1396.

29 V. Gray, A. Dreos, P. Erhart, B. Albinsson, K. Moth-Poulsen and M. Abrahamsson, *Phys. Chem. Chem. Phys.*, 2017, **19**, 10931–10939.

30 N. Harada, Y. Sasaki, M. Hosoyamada, N. Kimizuka and N. Yanai, *Angew. Chem. Int. Ed.*, 2020, **59**, 10252–10264.

31 M. Teders, C. Henkel, L. Anhäuser, F. Strieth-Kalthoff, A. Gómez-Suárez, R. Kleinmans, A. Kahnt, A. Rentmeister, D. Guldi and F. Glorius, *Nat. Chem.*, 2018, **10**, 981–988.

32 C. Kerzig and M. Goez, *Chem. Sci.*, 2016, **7**, 3862–3868.

33 K. Sandros, *Acta Chem. Scand.*, 1964, 18, 2355–2374.

34 C. Kerzig and O. S. Wenger, *Chem. Sci.*, 2019, **10**, 11023–11029.

35 D. Rehm and A. Weller, *Isr. J. Chem.*, 1970, **8**, 258–271.

36 S. M. Hubig and J. K. Kochi, *J. Am. Chem. Soc.*, 1999, **121**, 1688–1694.

37 C. Kerzig and M. Goez, *Phys. Chem. Chem. Phys.*, 2015, **17**, 13829–13836.

38 R. Naumann and M. Goez, *Green Chem.*, 2019, **21**, 4470–4474.

39 N. Periasamy and K. S. V. Santhanam, *Proc. Indian Acad. Sci. - Sect. A*, 1974, **80**, 194–206.

40 J. J. Warren, T. A. Tronic and J. M. Mayer, *Chem. Rev.*, 2010, **110**, 6961–7001.

41 S. Matsuoka, T. Kohzuki, C. Pac, A. Ishida, S. Takamuku, M. Kusaba, N. Nakashima and S. Yanagida, *J. Phys. Chem*, 1992, **96**, 4437–4442.

42 M. Zhao, W. Xie and C. Cui, *Chem. - Eur. J.*, 2014, **20**, 9259–9262.

43 C. Kerzig, M. Hoffmann and M. Goez, *Chem. - Eur. J.*, 2018, **24**, 3038–3044.